INTERNATIONAL JOURNAL FOR NUMERICAL METHODS IN ENGINEERING
Int. J. Numer. Meth. Engng 2000; **48**:1359–1400

A unified stability analysis of meshless particle methods

Ted Belytschko[*,†,‡], Yong Guo[§], Wing Kam Liu[¶] and Shao Ping Xiao[‖]

Department of Mechanical Engineering, Northwestern University, 2145 Sheridan Road, Evanston, IL 60208, U.S.A.

SUMMARY

A unified stability analysis of meshless methods with Eulerian and Lagrangian kernels is presented. Three types of instabilities were identified in one dimension: an instability due to rank deficiency, a tensile instability and a material instability which is also found in continua. The stability of particle methods with Eulerian and Lagrangian kernels is markedly different: Lagrangian kernels do not exhibit the tensile instability. In both kernels, the instability due to rank deficiency can be suppressed by stress points. In two dimensions the stabilizing effect of stress points is dependent on their locations. It was found that the best approach to stable particle discretizations is to use Lagrangian kernels with stress points. The stability of the least-squares stabilization was also studied. Copyright © 2000 John Wiley & Sons, Ltd.

KEY WORDS: particle methods; stability; kernel

1. INTRODUCTION

For a variety of problems with extremely large deformation, moving boundaries or discontinuities, mesh-free methods are very attractive. Mesh-free methods, which construct the approximation entirely in terms of nodes, are less susceptible to distortion difficulties than finite elements. The smoothed particle (SPH) method, which was used for modelling astrophysical phenomena [1, 2], is the oldest of these mesh-free methods. It uses kernel estimates to construct the approximation. Uncorrected kernel approximations appear to converge only when the size of the 'window' which determines the number of nodes that interact remains constant as the model is refined. Mas-Gallic and Raviart [3] proved convergence for this situation but Belytschko *et al.* [4] found that SPH

[*] Correspondence to: Ted Belytschko, Department of Mechanical Engineering, Northwestern University, 2145 Sheridan Road, Evanston, IL 60208, U.S.A.
[†] E-mail: t-belytschko@nwu.edu
[‡] Chair and Walter P. Murphy, Professor of Mechanical Engineering, Northwestern University
[§] Graduate student, Department of Civil Engineering, Northwestern University, 2145 Sheridan Road, Evanston, IL 60208, U.S.A.
[¶] Professor of Mechanical and Civil Engineering
[‖] Graduate student

Contract/grant sponsor: Army Research Office
Contract/grant sponsor: Office of Naval Research
Contract/grant sponsor: Army High Performance Computing Research Center; contract/grant number: DAAH04-95-2-003/ Contract DAAH04-95-C-0008

Received 1 July 1999
Revised 20 July 1999

does not converge when the support decreases proportionally to the particle spacing. Support sizes independent of refinement are very expensive since sparsity decreases markedly with refinement. Therefore a correction of the approximation [5] or the derivatives [6, 7] is crucial. The element-free Galerkin (EFG) method uses a moving least-squares approximation. It is equivalent to the Liu correction of the kernel and is consistent [8, 9]. Other meshless methods include reproducing kernel particle method (RKPM) [5, 10], particle-in-cell method [11, 12], *hp*-clouds [13, 14] and the partition of unity finite element (PUFEM) [15, 16].

The stability of particle methods is essential to their robustness. One of the most troublesome instabilities of the SPH method is the tensile instability. This instability was first identified by Swegle *et al.* [17] by a Neumann analysis of the one-dimensional equation. Subsequently, Dyka *et al.* [18, 19], motivated by similar difficulties in finite elements, where under-integration of the Galerkin form leads to spurious singular modes, recommended the insertion of additional quadrature points. They are called stress points since only the constitutive equation is evaluated at these points. Stress points have been implemented in multi-dimensions by Libersky and Randles [7]. Dilts [20] has argued that the tensile instability can be alleviated by the use of a moving least-squares approximation for the dependent variables and reported results which substantiated his claim. Swegle and co-workers have proposed a conservative smoothing scheme to eliminate the tensile instability [17, 22, 21]. Morris has examined the stability for multi-dimensional cases and suggested using higher-order spline kernels [23, 24]. Beissel and Belytschko [25], in earlier work on moving least-squares approximations, found that instabilities occurred with nodal integration of the Galerkin form of the momentum equation. These instabilities occurred in the absence of a large tensile stress. They developed a stabilization by addition of the square of the momentum equation to the weak form.

Clearly, several different instabilities occur in particle methods. The objective of this paper is to provide a unified stability analysis to clearly identify the various instabilities and the effectiveness of various stabilization techniques. Two distinct instabilities result from the discretization:

(i) a high-frequency instability which results from the rank deficiency of the discrete divergence operator;
(ii) a tensile instability which results from the interaction of the second derivative of kernel and the tensile stress, it occurs even in one-dimensional plane response.

It will be shown that the tensile instability is to a large extent the idiosyncrasy of what we call Eulerian kernels. In an Eulerian kernel, the stability depends on the stress and the second derivative of the kernel. This generates the tensile instability. We will show that when the kernel is a function of the material (Lagrangian) co-ordinates, a so-called Lagrangian kernel, the tensile instability does not occur.

On the other hand, an instability due to rank deficiency occurs for both Lagrangian and Eulerian kernels with nodal integration or collocation. This instability can be eliminated by stress points. However, it is found that stress points cannot completely stabilize Eulerian kernels.

We will compare the instabilities which are expected in a continuum to the instabilities in the particle methods. Only rate-independent materials will be considered. As part of this analysis, we will develop upper bounds for the maximum frequency of particle discretizations in one and two dimensions. This provides conservative estimates on the stable time steps for explicit methods.

The outline of this paper is as follows. In the next section, the governing equations for a continuous medium are given in the framework of a Lagrangian formulation. A stability analysis

of a continuum with rate-independent constitutive law is presented to illustrate the instabilities which are present in the partial differential equations for continua. The particle approximations are briefly described and used to obtain the discrete equations in Section 3. Different quadrature schemes and Lagrangian and Eulerian kernels are discussed. The stability properties of nodal integration and stress point integration with Eulerian and Lagrangian kernels are studied in a plane wave problem and a two-dimensional anti-plane wave problem. The least-squares stabilization by Beissel and Belytschko is also examined. In Section 5, upper bounds of the critical time step in Galerkin-type particle methods for explicit dynamic analysis are obtained. Several examples, including the Taylor bar normal impact and a fluid–structure interaction, are solved with EFG using nodal integration and stress points with a Lagrangian kernel. The results show that there is no instability in either solid or fluid, which verifies that stress points with a Lagrangian kernel suffice to eliminate the instabilities due to particle discretizations.

2. GOVERNING EQUATIONS

Consider a continuous body, which initially occupies the domain Ω_0 (called the reference configuration) and is currently in the configuration Ω. The motion is given by a mapping, $\mathbf{x} = \mathbf{x}(\mathbf{X}, t)$, which gives the position $\mathbf{x}$ of each material point $\mathbf{X}$ as a function of time. The map $\mathbf{x}(\mathbf{X}, t)$ between Ω_0 and Ω is assumed to be one-to-one and onto.

We will confine our investigation to isothermal, adiabatic processes, so the governing equations are the conservation of mass

$$\rho J = \rho_0 \tag{1}$$

conservation of linear momentum

$$\rho_0 \ddot{\mathbf{u}} = \rho_0 \mathbf{b} + \nabla_{\mathbf{X}} \cdot \mathbf{P} \tag{2}$$

conservation of angular momentum

$$\mathbf{F} \cdot \mathbf{P} = \mathbf{P}^{\mathrm{T}} \cdot \mathbf{F}^{\mathrm{T}} \tag{3}$$

and conservation of energy

$$\rho_0 \dot{\mathscr{E}} = \mathbf{P}^{\mathrm{T}} : \dot{\mathbf{F}} \tag{4}$$

In the above, ρ_0, ρ are, respectively, initial and current densities, $\mathbf{P}$ is the nominal stress tensor (the transpose of the first Piola–Kirchhoff stress), $\mathbf{F} = \mathbf{x} \overleftarrow{\nabla}_{\mathbf{X}} = \partial \mathbf{x} / \partial \mathbf{X}$ is the deformation gradient and $J = \det \mathbf{F}$, $\mathscr{E}$ is the internal energy per unit mass, and $\mathbf{b}$ is the body force per unit mass. The superimposed dot indicates the material time derivative t, e.g. $\ddot{\mathbf{u}} = \partial^2 \mathbf{u}(\mathbf{X}, t) / \partial t^2$, and the superscript T denotes transpose of a tensor or vector. The mass conservation Equation (1) is written in a Lagrangian form, where it is integrable and hence an algebraic equation. In SPH an Eulerian form of mass conservation is often used; this complicates the numerics and stability analysis and seems to provide no apparent benefits.

The boundary conditions are

$$u_i(\mathbf{X}, t) = \bar{u}_i(\mathbf{X}, t), \quad \mathbf{X} \in \Gamma_0^u \tag{5}$$

$$\mathbf{n}^0(\mathbf{X}) \cdot \mathbf{P}(\mathbf{X}, t) = \bar{\mathbf{t}}(\mathbf{X}, t), \quad \mathbf{X} \in \Gamma_0^t \tag{6}$$

where $\bar{\mathbf{u}}$ and $\bar{\mathbf{t}}$ are the prescribed displacement and traction, respectively, and $\mathbf{n}^0$ is the outward normal of the boundary in the reference configuration, and Γ_0^u, Γ_0^t are disjoint subsets of the boundary Γ_0, i.e. $\Gamma_0 = \Gamma_0^u \cup \Gamma_0^t$ and $\emptyset = \Gamma_0^u \cap \Gamma_0^t$.

The constitutive equation must be posed in terms of frame-invariant (objective) rates, so we use a relation between the rates of the second Piola–Kirchhoff stress $\mathbf{S}$ and the Green strain $\mathbf{E}$,

$$\dot{\mathbf{S}} = \mathbf{C}^{\mathrm{SE}} : \dot{\mathbf{E}} \tag{7}$$

where $\mathbf{C}^{\mathrm{SE}}$ is the material tangent modulus. The measures of stress rate and strain rate related by the particular tangent modulus are identified by a superscript in the above because other stress and strain rates will be used subsequently and the tangent moduli for those are different. The Green strain $\mathbf{E}$ is given by

$$\mathbf{E} = \tfrac{1}{2}(\mathbf{F}^{\mathrm{T}}\mathbf{F} - \mathbf{I}) \tag{8}$$

The nominal stress is related to the second Piola–Kirchhoff stress by

$$\mathbf{P} = \mathbf{S}\mathbf{F}^{\mathrm{T}} \tag{9}$$

It should be noted that the usual Eulerian forms of the continuity and momentum equations are simply transformations of the above and possess identical stability properties.

2.1. Stability analysis for continuum

For the purpose of providing some guidelines as to what type of instability to expect, we summarize here a standard stability analysis of the continuum [26–28]. Note that only the momentum equation needs to be considered for a Lagrangian treatment, since the mass conservation equation is algebraic; the energy equation is irrelevant in an isothermal, adiabatic process. We will assume that the body forces vanish.

The governing equations for the large deformation of continuum are non-linear. In order to conduct a stability analysis, we first derive the linearized equations. Assume perturbations in the displacement

$$\tilde{\mathbf{u}} = \mathbf{u} + \tilde{\mathbf{u}} \tag{10}$$

where the superposed $\sim$ denotes a perturbation. The perturbation solutions are governed by the following equation:

$$\rho_0 \ddot{\tilde{\mathbf{u}}} = \nabla_{\mathbf{X}} \cdot \tilde{\mathbf{P}} \tag{11}$$

From Equations (7)–(9), it follows that

$$\tilde{\mathbf{P}} = \tilde{\mathbf{S}}\mathbf{F}^{\mathrm{T}} + \mathbf{S}\tilde{\mathbf{F}}^{\mathrm{T}} = \mathbf{C}^{\mathrm{SE}} : (\mathbf{F}^{\mathrm{T}}\tilde{\mathbf{F}})\mathbf{F}^{\mathrm{T}} + \mathbf{S}\tilde{\mathbf{F}}^{\mathrm{T}} \tag{12}$$

In the above we have used the rate form of the constitutive equation and the minor symmetry of the material modulus $\mathbf{C}^{\mathrm{SE}}$

$$\tilde{\mathbf{S}} = \mathbf{C}^{\mathrm{SE}} : \tilde{\mathbf{E}} = \mathbf{C}^{\mathrm{SE}} : (\mathbf{F}^{\mathrm{T}}\tilde{\mathbf{F}}) \tag{13}$$

Writing (12) in indicial form, the perturbed stress is given by

$$\tilde{P}_{ij} = C^{\mathrm{SE}}_{ikab} F^{\mathrm{T}}_{ar} \tilde{F}_{rb} F^{\mathrm{T}}_{kj} + S_{ib}\tilde{F}^{\mathrm{T}}_{bj} = F_{ra}F_{jk}C^{\mathrm{SE}}_{ikab}\tilde{F}_{rb} + S_{ib}\tilde{F}_{jb} = A^0_{ijrb}\tilde{F}_{rb} \tag{14}$$

The above defines the first elasticity tensor $\mathbf{A}^0$ as

$$A^0_{ijrb} = F_{ra}F_{jk}C^{\mathrm{SE}}_{ikab} + S_{ib}\delta_{jr} \tag{15}$$

The governing equation in terms of the perturbed displacements can be obtained by substituting Equation (14) into (11):

$$\rho_0 \frac{\partial^2 \tilde{u}_i}{\partial t^2}(\mathbf{X}, t) = \frac{\partial}{\partial X_j}[A^0_{jirb}(\mathbf{X}, t)\tilde{F}_{rb}(\mathbf{X}, t)] = \frac{\partial}{\partial X_j}\left(A^0_{jirb}\frac{\partial \tilde{u}_r}{\partial X_b}\right) \tag{16}$$

Assume that the perturbation of displacements is in the form of a plane wave

$$\tilde{\mathbf{u}} = \mathbf{g}\mathrm{e}^{\omega t + \mathrm{i}\kappa \mathbf{n}^0 \cdot \mathbf{X}} \equiv \mathbf{g}\mathrm{e}^{\alpha(\mathbf{X}, t)} \tag{17}$$

where κ is the wave number, ω is a complex frequency and $\mathbf{n}^0$ is the normal direction of the wavefront with respect to the initial configuration. Then

$$\tilde{F}_{rb} = \frac{\partial \tilde{u}_r}{\partial X_b} = \mathrm{i}\kappa g_r n^0_b \mathrm{e}^{\alpha(\mathbf{X}, t)} \tag{18}$$

and

$$\frac{\partial}{\partial X_j}(A^0_{jirb}\tilde{F}_{rb}) = \mathrm{i}\kappa A^0_{jirb} g_r n^0_b \, \mathrm{i}\kappa n^0_j \mathrm{e}^{\alpha(\mathbf{X}, t)} = -\kappa^2 A^0_{jirb} n^0_b n^0_j g_r \mathrm{e}^{\alpha(\mathbf{X}, t)} \tag{19}$$

Since

$$\frac{\partial^2 \tilde{u}_i}{\partial t^2} = \omega^2 g_i \mathrm{e}^{\alpha(\mathbf{X}, t)} \tag{20}$$

the perturbed equation (16) yields

$$\rho_0 \omega^2 g_i + \kappa^2 A^0_{jirb} n^0_b n^0_j g_r = 0 \quad \text{for } i = 1 \text{ to } n_{\mathrm{SD}} \tag{21}$$

or

$$\left(\frac{\omega^2}{\kappa^2}\delta_{ir} + \frac{1}{\rho_0}\mathscr{A}^0_{ir}\right) g_r = 0, \quad \mathscr{A}^0_{ir} = A^0_{jirb} n^0_b n^0_j \tag{22}$$

Thus, the characteristic equation for the continuum medium is

$$\det\left[\frac{\omega^2}{\kappa^2}\delta_{ir} + \frac{1}{\rho_0}\mathscr{A}^0_{ir}\right] = 0 \tag{23}$$

If the matrix $\mathscr{A}^0$ is positive definite, then the roots ω must be imaginary and the continuum is stable. Note that instabilities can occur when $\mathscr{A}^0$ loses positive definiteness, which can occur

when $\mathbf{C}^{\mathrm{SE}}$ loses positive definiteness in $\mathbf{C}^{\mathrm{SE}}$ due to strain-softening or with absence of the major symmetry $C^{\mathrm{SE}}_{ikab} = C^{\mathrm{SE}}_{abik}$, i.e. a non-associative law.

Equation (23) can be used to obtain the stability condition in terms of Eulerian variables by letting the current configuration be the reference configuration. This gives $\mathbf{F} = \mathbf{I}$, $\mathbf{S} = \boldsymbol{\sigma}$ (the Cauchy stress), $\dot{\mathbf{S}} = \boldsymbol{\sigma}^{\nabla \mathscr{T}}$ (the Truesdell rate) and $\mathbf{C}^{\mathrm{SE}} = \mathbf{C}^{\sigma\mathscr{T}}$, where $\mathbf{C}^{\sigma\mathscr{T}}$ is the modulus relating the Truesdell rate of the Cauchy stress to the rate of deformation, see Belytschko *et al.* [29]. Then

$$\det\left[\frac{\omega^2}{\kappa^2}\delta_{ir} + \frac{1}{\rho}\mathscr{A}_{ir}\right] = 0 \tag{24}$$

where

$$\mathscr{A}_{ir} = A_{jirb} n_b n_j, \quad A_{ijrb} = C^{\sigma\mathscr{T}}_{ikab} + \sigma_{ib}\delta_{jr} \tag{25}$$

2.2. *One-dimensional stability analysis*

For simplicity, we consider the same stability anlysis in one dimension: a plane wave in the X-direction. The governing equations in one dimension are

$$\rho_0 \ddot{u} = \frac{\partial P}{\partial X} + \rho_0 b \tag{26}$$

$$P = SF, \quad \dot{S} = C^{\mathrm{SE}}\dot{E} = C^{\mathrm{SE}} F \dot{F}, \quad F = \frac{\partial x}{\partial X} = \frac{\partial u}{\partial X} + 1 \tag{27}$$

The equations for the perturbed solutions corresponding to Equations (11)–(14) are

$$\rho_0 \ddot{\tilde{u}} = \frac{\partial \tilde{P}}{\partial X} \tag{28}$$

$$\tilde{P} = \bar{C}^{\mathrm{SE}}\tilde{F} = \bar{C}^{\mathrm{SE}}\frac{\partial \tilde{u}}{\partial X}, \quad \bar{C}^{\mathrm{SE}} = C^{\mathrm{SE}}F^2 + S \tag{29}$$

where $\tilde{u}$ is the perturbed displacement in the x-direction, $\tilde{P}$, $\tilde{F}$, F, and S are the '11' components of the corresponding tensors. The linearized equation in terms of the perturbed displacement can be written as

$$\rho_0 \frac{\partial^2 \tilde{u}}{\partial t^2} = \frac{\partial}{\partial X}\left(\bar{C}^{\mathrm{SE}}\frac{\partial \tilde{u}}{\partial X}\right) = \bar{C}^{\mathrm{SE}}\frac{\partial^2 \tilde{u}}{\partial X^2} \tag{30}$$

We use a Fourier representation of the perturbed solution

$$\tilde{u} = g e^{\mathrm{i}\kappa X + \mathrm{i}\omega t} \tag{31}$$

Substituting the above into (30) yields that the stability is governed by

$$\omega^2 = \frac{\bar{C}^{\mathrm{SE}}\kappa^2}{\rho_0} \tag{32}$$

It can be seen that the solution becomes unstable only when $\bar{C}^{\mathrm{SE}} \leqslant 0$. The threshold for unstable behaviour is

$$\bar{C}^{\mathrm{SE}} = S + C^{\mathrm{SE}}F^2 = 0 \tag{33}$$

In current congifuration, $\tilde{P} = \bar{C}^{\sigma\mathscr{T}} F^{-1} \tilde{F}$ and $\bar{C}^{\sigma\mathscr{T}} = (\sigma + C^{\sigma\mathscr{T}})$. The above condition becomes

$$\sigma + C^{\sigma\mathscr{T}} = 0 \tag{34}$$

The above equality between $\bar{C}^{\mathrm{SE}}$ and $\bar{C}^{\sigma\mathscr{T}}$ is included to stress that for a particular material, the two tangent moduli must be equivalent. The instability can occur whenever $\bar{C}^{\mathrm{SE}}$ (or $\bar{C}^{\sigma\mathscr{T}}$) vanishes, which occurs in two situations:

(i) under tensile stress when $C^{\sigma\mathscr{T}}$ becomes sufficiently negative (this corresponds to the well-known instability in strain softening);
(ii) under compressive stress when the $C^{\sigma\mathscr{T}} = |\sigma|$.

We will see that in certain particle methods, instabilities can also occur under a tensile stress or in the absence of stress when $C^{\sigma\mathscr{T}} > 0$. These are instabilities due to deficiencies in the discretization.

3. DISCRETE EQUATIONS

3.1. Meshless and particle approximations

In meshless methods, all dependent variables are approximated by

$$u(\mathbf{X}, t) = \sum_{J \in \mathscr{N}(\mathbf{X})} \phi_J(\mathbf{X}) u_J(t) \tag{35}$$

where u_J is the nodal value at the particle $\mathbf{X}_J$, $\mathscr{N}(\mathbf{X})$ is the set of particles contributing to the evaluated point $\mathbf{X}$, and $\phi_J(\mathbf{X})$ is the approximation function. The function ϕ_J is sometimes called a shape function. In general, it does not have the interpolation property, i.e. $\phi_I(\mathbf{X}_J) \neq \delta_{IJ}$ and consequently $u_I \neq u(\mathbf{X}_I)$. Therefore special treatment of essential boundary conditions is required [8, 30].

A large class of particle methods can be generated by using various shape functions. In the element-free Galerkin method (EFG), the shape functions are moving least-squares (MLS) approximations [9],

$$\mathbf{\Phi} = [\phi_1(\mathbf{X}) \;\; \phi_2(\mathbf{X}) \;\; \cdots \;\; \phi_N(\mathbf{X})] = \mathbf{p}^{\mathrm{T}}(\mathbf{X}) \mathbf{A}^{-1}(\mathbf{X}) \mathbf{B}(\mathbf{X}) \tag{36}$$

where

$$\mathbf{A} = \sum_{J \in \mathscr{N}(\mathbf{X})} W_J(\mathbf{X}, h) \mathbf{p}(\mathbf{X}_J - \mathbf{X}) \mathbf{p}^{\mathrm{T}}(\mathbf{X}_J - \mathbf{X}) \tag{37}$$

$$\mathbf{B} = [W_1(\mathbf{X}) \mathbf{p}(\mathbf{X}_1 - \mathbf{X}) \quad W_2(\mathbf{X}) \mathbf{p}(\mathbf{X}_2 - \mathbf{X}) \;\; \cdots \;\; W_N(\mathbf{X}) \mathbf{p}(\mathbf{X}_N - \mathbf{X})] \tag{38}$$

and N is the total number of nodes within the domain of influence at point $\mathbf{X}$, designated by the set $\mathscr{N}(\mathbf{X})$. $W(\mathbf{X}, h)$ is the weight function, usually of compact support and

$$W_J(\mathbf{X}, h) = W(\mathbf{X} - \mathbf{X}_J, h) \tag{39}$$

Here h is the size of the support or smoothing length, which is determined by a dilation parameter D_{mx}, e.g. $h = D_{\mathrm{mx}} \Delta X$ for uniformly spaced particles in one dimension; $\mathbf{p}(\mathbf{X})$ is a vector of basis functions, usually consisting of polynomial functions to a specific order. The linear polynomial

basis functions in two dimensions include $\mathbf{p}^{\mathrm{T}} = [1\ X\ Y]$ and suffice for convergence of second-order PDEs such as results from combining (2) with a constitutive equation. In the above computation, a shift of origin is made at the evaluation point to improve the conditioning of the $\mathbf{A}$ matrix and to minimize the roundoff error. The gradient of a field variable in EFG is

$$\nabla_{\mathbf{X}} u = \sum_J \nabla_{\mathbf{X}} \phi_J(\mathbf{X}) u_J \tag{40}$$

Fast methods for this computation are given in Belytschko *et al.* [31].

The smoothed particle hydrodynamics (SPH) approximations are based on a kernel approximation and constructed as [32]

$$u(\mathbf{X}) = \sum_J V_J^0 W_J(\mathbf{X}, h) u_J, \quad \phi_J(\mathbf{X}) = V_J^0 W_J(\mathbf{X}, h) \tag{41}$$

where V_J^0 is the initial volume of the particle $\mathbf{X}_J$, $W(\mathbf{X}, h)$ is the kernel function with smoothing length h. The kernel in SPH and the weight function in EFG play identical roles. Instead of directly taking derivatives of Equation (41), the gradient of a field variable in SPH is calculated by

$$\nabla_{\mathbf{X}} u = -\sum_J V_J^0 \nabla_{\mathbf{X}'} W_J(\mathbf{X}, h) u_J \tag{42}$$

which results from integration by parts and

$$\nabla_{\mathbf{X}'} W_J(\mathbf{X}, h) = \nabla_{\mathbf{X}'} W(\mathbf{X} - \mathbf{X}', h)|_{\mathbf{X}'=\mathbf{X}_J} \tag{43}$$

Since

$$\nabla_{\mathbf{X}'} W_J(\mathbf{X}, h) = -\nabla_{\mathbf{X}} W_J(\mathbf{X}, h) \tag{44}$$

Equation (42) can be written as

$$\nabla_{\mathbf{X}} u = \sum_J V_J^0 \nabla_{\mathbf{X}} W_J(\mathbf{X}, h) u_J \tag{45}$$

Therefore, the gradient of the shape function in Equation (41) is equivalent to the term in Equation (45). Other formulas have been proposed to estimate the gradient of a field in SPH [32, 7]. Three commonly used forms are

$$\nabla_{\mathbf{X}} u_I = \sum_J \frac{m_J}{\rho_{0J}} u_J \nabla_{\mathbf{X}} W_{IJ} \tag{46}$$

$$\nabla_{\mathbf{X}} u_I = \frac{1}{\rho_{0I}} \sum_J m_J (u_J - u_I) \nabla_{\mathbf{X}} W_{IJ} \tag{47}$$

$$\nabla_{\mathbf{X}} u_I = \rho_{0I} \sum_J m_J \left(\frac{u_I}{\rho_{0I}^2} + \frac{u_J}{\rho_{0J}^2} \right) \nabla_{\mathbf{X}} W_{IJ} \tag{48}$$

where $m = \rho_0 V^0$ and

$$W_{IJ} = W(\mathbf{X}_I - \mathbf{X}_J, h), \quad \nabla_{\mathbf{X}} W_{IJ} = \nabla_{\mathbf{X}} W(\mathbf{X} - \mathbf{X}_J, h)|_{\mathbf{X}=\mathbf{X}_I} \tag{49}$$

Randles and Libersky [7] reported that (47) is more accurate than (46) since the gradient of u is more explicit and thus is less susceptible to particle disorder. When (48) is applied to the

momentum equation, the linear and angular momentum are conserved exactly, since the particle forces are equal and opposite and act along the line joining their centres (provided that the kernel is symmetric) [33].

3.2. Discrete equations with particle methods

3.2.1. Galerkin method. The discrete equations in EFG and RKPM are obtained from the Galerkin weak forms. The weak form of the linear momentum conservation can be written as

$$\int_{\Omega_0} \rho_0 \delta\mathbf{u} \cdot \ddot{\mathbf{u}} \, \mathrm{d}\Omega = \int_{\Omega_0} \rho_0 \delta\mathbf{u} \cdot \mathbf{b} \, \mathrm{d}\Omega - \int_{\Omega_0} \nabla_{\mathbf{X}} \delta\mathbf{u} : \mathbf{P} \, \mathrm{d}\Omega + \int_{\Gamma_0^t} \delta\mathbf{u} \cdot \bar{\mathbf{t}} \, \mathrm{d}\Gamma \tag{50}$$

where $\delta\mathbf{u} \in \mathscr{U}_0$ is the test function with $\mathscr{U}_0 = \{\mathbf{u} \mid \mathbf{u} \in C^0,\ u_i(\mathbf{X}, t) = 0 \text{ for } \mathbf{X} \in \Gamma_0^u\}$.

Substituting the particle approximation (35) into (50) and using a diagonal mass matrix, we have

$$m_I \ddot{\mathbf{u}}_I = \mathbf{f}_I^{\text{ext}} - \mathbf{f}_I^{\text{int}}, \quad m_I = \rho_0 V_I^0 \tag{51}$$

where $\mathbf{f}_I^{\text{ext}}$, $\mathbf{f}_I^{\text{int}}$ are the external and internal nodal forces, respectively, given by

$$\mathbf{f}_I^{\text{ext}} = \int_{\Omega_0} \rho_0 \phi_I \mathbf{b} \, \mathrm{d}\Omega + \int_{\Gamma_0^t} \phi_I \bar{\mathbf{t}} \, \mathrm{d}\Gamma \tag{52}$$

$$\mathbf{f}_I^{\text{int}} = \int_{\Omega_0} \nabla_{\mathbf{X}} \phi_I \cdot \mathbf{P} \, \mathrm{d}\Omega \tag{53}$$

It has been shown that the above exactly conserve linear and angular momentum [4], because of the linear completeness of the approximation. However, as pointed out by Dilts [20], this discretization does not conserve momentum for a particle pair.

3.2.2. Collocation method. In standard SPH, the discrete equations are constructed by collocation, i.e. enforcing the kernel approximation to the governing equations at each particle in the domain. For example, the linear momentum equation without body force, Equation (2), is discretized to

$$\rho_{0I} \ddot{\mathbf{u}}_I = (\nabla_{\mathbf{X}} \cdot \mathbf{P})_I \tag{54}$$

Using (46) for the gradient of the stress, we can write the collocation equation

$$m_I \ddot{\mathbf{u}}_I = V_I^0 \sum_J V_J^0 \nabla_{\mathbf{X}} W_{IJ} \cdot \mathbf{P}_J \tag{55}$$

The above discrete equation is identical to Equation (51) when we define the internal nodal force by

$$\mathbf{f}_I^{\text{int}} = -V_I^0 \sum_J V_J^0 \nabla_{\mathbf{X}} W_{IJ} \cdot \mathbf{P}_J \tag{56}$$

The above collocation discrete equations are equivalent to nodal integration of Galerkin forms, Equation (53), provided that the kernel is symmetric and the smoothing lengths for all particles are identical, this is further examined in Reference [4]. However, a theoretical framework for the simple treatment of traction (natural) boundary conditions is not available in collocation methods.

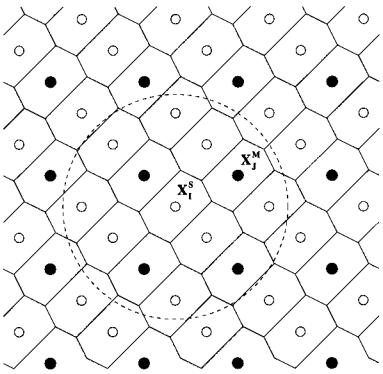

Figure 1. Stress point integration with Voronoi cells for quadrature; ○ is stress point.

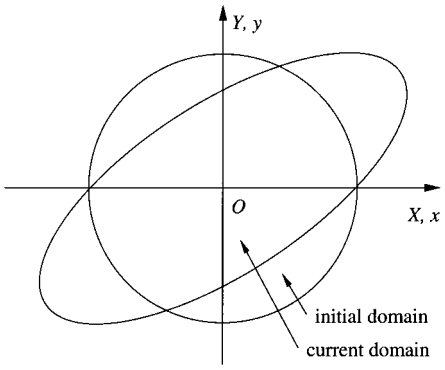

Figure 2. Domain of influence in material and spatial co-ordinates with deformation $x = X + 2Y$, $y = Y$.

3.3. Integration schemes

In the EFG method, the integrals (52), (53) are usually evaluated over background cells based on an octree structure [8]. Full quadrature in the cells is computationally expensive for non-linear and/or dynamic problems. Nodal integration [25], in which the integrals are computed from nodal values and is truly meshless, has stability properties similar to SPH. SPH collocation is equivalent to EFG method with nodal integration in most cases, so it will exhibit the same instabilities.

3.3.1. Nodal integration. With nodal quadrature, the quadrature points are the nodal points. The internal nodal forces, Equation (53), are computed by

$$\mathbf{f}_I^{\text{int}} = \sum_J V_J^0 \nabla_{\mathbf{X}} \phi_I(\mathbf{X}_J) \cdot \mathbf{P}_J \tag{57}$$

As mentioned previously, the discrete momentum equation in the collocated SPH is identical to that in EFG with nodal integration.

3.3.2. Stress point integration. One approach to stabilizing both SPH and nodal quadrature is to use additional quadrature points called stress points. They are called stress points since the stresses need to be calculated at these points by the constitutive equation in terms of the master node velocities.

Stress points were proposed by Dyka *et al.* [18, 19] and Randles and Libersky [7]. In stress point integration, particles are added to the original set of particles; the original particles are called master nodes, (see Figure 1), whereas the stress points can also be called slave particles. This nomenclature originates in finite element methods, where slave nodes are nodes whose motion is determined by the motion of master nodes through kinematic relations. The slave particles are used only for the integration of the Galerkin weak form (or computation of acceleration for the collocated momentum equation in SPH). The kinematic values of slave nodes, such as velocity, are evaluated from the neighbouring master nodes. The displacement and velocity at the

slave particles (stress points) are

$$\mathbf{u}_I^S = \sum_J \phi_J(\mathbf{X}_I^S)\mathbf{u}_J^M, \quad \mathbf{v}_I^S = \sum_J \phi_J(\mathbf{X}_I^S)\mathbf{v}_J^M \tag{58}$$

where $\phi_J(\mathbf{X}_I^S)$ is the shape function of the supporting master node J at stress point $\mathbf{X}_I^S$.

The internal nodal forces, Equation (53), are then calculated as

$$\mathbf{f}_I^{\text{int}} = \sum_{J\in\mathcal{N}_M} V_J^{0M}\nabla_{\mathbf{X}}\phi_I(\mathbf{X}_J^M)\cdot\mathbf{P}_J^M + \sum_{J\in\mathcal{N}_S} V_J^{0S}\nabla_{\mathbf{X}}\phi_I(\mathbf{X}_J^S)\cdot\mathbf{P}_J^S \tag{59}$$

where $\mathcal{N}_M$, $\mathcal{N}_S$ are sets of master nodes and stress points, respectively, which contribute to the master node $\mathbf{X}_I^M$, and the volumes V_J^{0M} and V_J^{0S} are computed from Voronoi diagram (see Figure 1) such that

$$\sum_J^{N_M} V_J^{0M} + \sum_J^{N_S} V_J^{0S} = V^0 \tag{60}$$

In the above, V^0 is the total initial volume and N_M and N_S is the number of master nodes and stress points in the model, respectively. Note that the volume for the master nodes in the integration, V_I^{0M}, differs from the volume associated with the mass, V_I^0, as in Equation (51). The second term on the RHS of (59) is the contribution of the slave particle stresses to the master node forces; the formulas are obtained by energy equivalence as described in Reference [29].

3.4. Eulerian and Lagrangian kernels

The kernel approximation to the motion $\mathbf{x} = \mathbf{x}(\mathbf{X}, t)$ can be written in two forms. In the first the kernel is a function of the material (Lagrangian) co-ordinates in the initial configuration

$$\begin{aligned}\mathbf{v}(\mathbf{X}, t) = \dot{\mathbf{x}}(\mathbf{X}, t) &= W(\mathbf{X} - \mathbf{X}_J, h)\mathbf{v}(\mathbf{X}_J, t)\\ &= W(\mathbf{X} - \mathbf{X}_J, h)\mathbf{v}_J(t), \quad \mathbf{X}\in\Omega_0\end{aligned} \tag{61}$$

while in the second form the kernel is a function of spatial (Eulerian) co-ordinates in the current configuration

$$\begin{aligned}\mathbf{v}(\mathbf{X}, t) = \dot{\mathbf{x}}(\mathbf{X}, t) &= W(\mathbf{x} - \mathbf{x}_J, h)\circ\mathbf{x}^{-1}\,\mathbf{v}(\mathbf{X}_J, t)\\ &= w(\mathbf{x} - \mathbf{x}_J, h)\mathbf{v}_J(t), \quad \mathbf{X}\in\Omega_0\end{aligned} \tag{62}$$

In both of the above $W(\mathbf{X}, h) > 0$ in a small subdomain called the domain of influence; it is often said that $W(\mathbf{X}, h)$ is of compact support. Usually, the domain of influence is spherical and the kernel is a function of the distance from the node, i.e.

$$W_J(\mathbf{X}) = W(s, h) \quad \text{where } s = \begin{cases}\|\mathbf{X} - \mathbf{X}_J\| & \text{for Lagrangian kernel}\\ \|\mathbf{x} - \mathbf{x}_J\| & \text{for Eulerian kernel}\end{cases} \tag{63}$$

It should be noted that in the first line of (62), when the spatial derivative of the kernel is needed, we are tacitly referring to the composition $W\circ\mathbf{x}^{-1}$.

We shall show that the stability characteristics of the two types of approximations are quite different. The Lagrangian kernel, Equation (61), is a function of material co-ordinates. As a consequence, the neighbours of a particle remain neighbours throughout the simulation unless a technique such as the visibility criterion is used to severe a connection [9]. This invariance of neighbours detracts somewhat from the versatility of the particle method. However, it has superior stability properties, in particular, as we will show, it does not suffer from the tensile instability. The severance of connectivity occurs due to constitutive behaviour. This is more representative of physical behaviour of materials than the procedures currently used in particle methods.

For a Lagrangian kernel, the shape of the support (domain of influence) changes with time. If the initial support is a ball, the current domain of influence can be substantially distorted (see Figure 2 in two-dimensional case). Whether this distortion is deleterious to the performance of the method is not clear at this time. However, the representation of the kernel in terms of the material co-ordinates does provide a more consistent procedure for dealing with fracture since, as we will show, separation by tensile instability is precluded.

The kernel in form (62) employs a spatial domain which maintains the same shape in space during the simulation; the smoothing length $h(t)$ can be made to vary with time [24].

4. STABILITY ANALYSIS OF PARTICLE EQUATIONS

4.1. Nodal quadrature in plane wave

In the following, we describe a linearized stability analyses of the discrete equations for SPH and EFG; this is equivalent to what is often called a von Neumann stability analysis. We consider an infinite slab under a uniform state of stress. The solution is perturbed by harmonics of various wavelengths. We consider the response stable if it decays or remains constant in amplitude, and unstable if it grows. A response is asymptotically stable if it decays to zero as time goes to infinity. This is a classical linearized stability analysis (see [34, 35]), and although the conditions are highly idealized, it yields a mathematically tractable problem that reveals a wealth of information about the stability of a discretization. The MLS approximation in EFG is identical to SPH discretization (3.12) for uniformly spaced interior nodes.The subsequent analysis applies to both Galerkin methods, such as EFG, and collocation methods, such as classical SPH, since in the stability analysis the domain is infinite, so the treatment of boundary conditions has no effect.

4.1.1. Eulerian kernel. For a plane wave in the x-direction, the only non-trivial components of the relevant tensors are the xx components. Thus, $J = F_{11} \equiv F$ (we drop the subscripts in the following) and consequently

$$\sigma = \frac{1}{J} FP = P \tag{64}$$

In EFG with an Eulerian kernel, the internal nodal force is given by

$$f_I^{\text{int}} = \int_\Omega \phi_I'(x)\sigma(x)\,\mathrm{d}\Omega \tag{65}$$

For nodal integration, the above integral is evaluated by summing the integrand at the nodes. The internal nodal force is then

$$f_I^{\text{int}} = \sum_J V_J \phi_I'(x_J)\sigma_J, \quad V_J = \frac{m_J}{\rho_J} = \frac{m_J F_J}{\rho_{0J}} \tag{66}$$

Thus, the discrete equations are

$$m_I \ddot{u}_I = f_I^{\text{ext}} - \sum_J \frac{m_J}{\rho_{0J}} \phi_I'(x_J)\sigma_J F_J \tag{67}$$

$$F_I = \frac{1}{1 - \left.\dfrac{\partial u}{\partial x}\right|_I}, \quad \left.\frac{\partial u}{\partial x}\right|_I = \sum_J \phi_J'(x_I) u_J \tag{68}$$

We consider the Fourier form of a perturbation in displacement

$$\tilde{u}_I = g e^{\mathrm{i}\kappa I \Delta X + \mathrm{i}\omega t} \tag{69}$$

and identify all perturbations by a superposed $\sim$. The perturbed equation is

$$m_I \ddot{\tilde{u}}_I = -\sum_J \frac{m_J}{\rho_{0J}} [\phi_I'(x_J)(\tilde{\sigma}_J F_J + \sigma_J \tilde{F}_J) + \sigma_J F_J \tilde{\phi}_I'(x_J)] \tag{70}$$

where

$$\tilde{\phi}_I'(x_J) = \phi_I''(x_J)(\tilde{u}_J - \tilde{u}_I) \tag{71}$$

The perturbed stress $\tilde{\sigma}_I$ is given by the linearized constitutive equation (29):

$$\tilde{\sigma}_I = \tilde{P}_I = \bar{C}_I^{\sigma\mathscr{T}} F_I^{-1} \tilde{F}_I \tag{72}$$

where $\bar{C}^{\sigma\mathscr{T}}$ are the moduli for the Truesdell rate. The perturbed deformation gradient $\tilde{F}_I$ is obtained from the definition (27)

$$\tilde{F}_I = \left.\frac{\partial \tilde{u}}{\partial X}\right|_I = F_I \sum_J \phi_J'(x_I)\tilde{u}_J \tag{73}$$

Substituting (69) into (70) and (73) gives the dispersion equation which for a symmetric weight function and identical particles is

$$\omega^2 = \frac{\bar{C}^{\sigma\mathscr{T}}}{\rho} \left[\sum_j \phi'(j\Delta x)\sin(\kappa j \Delta x)\right]^2 - \frac{\sigma}{\rho}\left\{\sum_j \phi''(j\Delta x)[1 - \cos(\kappa j \Delta x)] - \left[\sum_j \phi'(j\Delta x)\sin(\kappa j \Delta x)\right]^2\right\} \tag{74}$$

where $\bar{C}^{\sigma\mathscr{T}}$ is the counterpart of $\bar{C}^{\text{SE}}$ in (29) in the current configuration ($\bar{C}^{\text{SE}} = 0$ when $C^{\sigma\mathscr{T}} = 0$):

$$\bar{C}^{\sigma\mathscr{T}} = (C^{\sigma\mathscr{T}} + \sigma) \tag{75}$$

The response is unstable if the imaginary part of ω is negative, i.e. if $\text{Im}(\omega) < 0$.

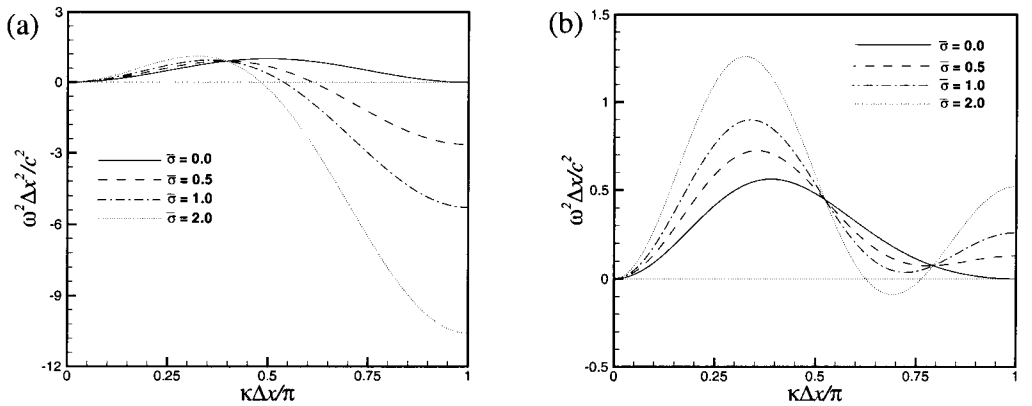

Figure 3. Frequency–wave number relations in plane wave by EFG with nodal integration and Eulerian kernel $c^2 = C^{\sigma\mathscr{T}}/\rho$: (a) $D_{\mathrm{mx}} = 1.5$; and (b) $D_{\mathrm{mx}} = 2.5$.

Comparing the above with the continuum stability equation (32), we see that the discrete stability equation contains a second term proportional to σ which is absent in the continuum stability equation; furthermore, the first term is modified by a sinusoid. The above equation indicates that there are three instabilities for the Eulerian kernel particle method:

(i) when the material is unstable, i.e. $\bar{C}^{\sigma\mathscr{T}}$ vanishes, which corresponds to the instability for the continuum;
(ii) the spurious singular mode $u_I = (-1)^I$ at the cutoff at wavenumber $\kappa = \pi/\Delta x$;
(iii) when $\sigma > 0$ and $\bar{C}^{\sigma\mathscr{T}} \neq 0$, this is the tensile instability identified by Swegle [21].

The first should occur in the discrete model since it occurs in the continuum. The second and third result from the discretization.

Figure 3 shows the frequency–wave number relations as a function of the normalized stress ($\bar{\sigma} = \sigma/C^{\sigma\mathscr{T}}$) for different support sizes ($h = D_{\mathrm{mx}}\Delta x$), for a quartic spline weight function. For $D_{\mathrm{mx}} = 1.5$, the frequency becomes imaginary for tensile stress if the wave number κ is greater than about $0.6\pi/\Delta x$ (the exact value depends on $\bar{\sigma}$), indicating a tensile instability. For $D_{\mathrm{mx}} = 2.5$, as seen in Figure 3, the tensile stress required for the onset of instability is greater. But the tensile instability remains.

An instability also occurs in the absence of stress, i.e. when $\sigma = 0$. This is called a spurious singular mode since $\omega = 0$ but the mode, shown in Figure 5, is obviously not a rigid-body translation. When $\omega = 0$, for a mode other than a rigid-body mode, the unstable mode is spurious. It is a weak instability which grows linearly with time. It is called a rank-deficient mode because it reflects a rank deficiency in the stiffness matrix $\mathbf{K}$ in the linearized equilibrium equations

$$\Delta\mathbf{f}^{\mathrm{int}} \equiv \mathbf{K}\Delta\mathbf{d} = \Delta\mathbf{f}^{\mathrm{ext}} \tag{76}$$

This instability is distinct from the tensile instability. It also occurs in SPH, since the discrete equations in this case are identical. As shown in Figure 4, when $\bar{\sigma} = -1$, i.e when $\bar{C}^{\sigma\mathscr{T}} = 0$ the discrete equations are also unstable for most wave numbers. This instability occurs in the continuum for all wave numbers.

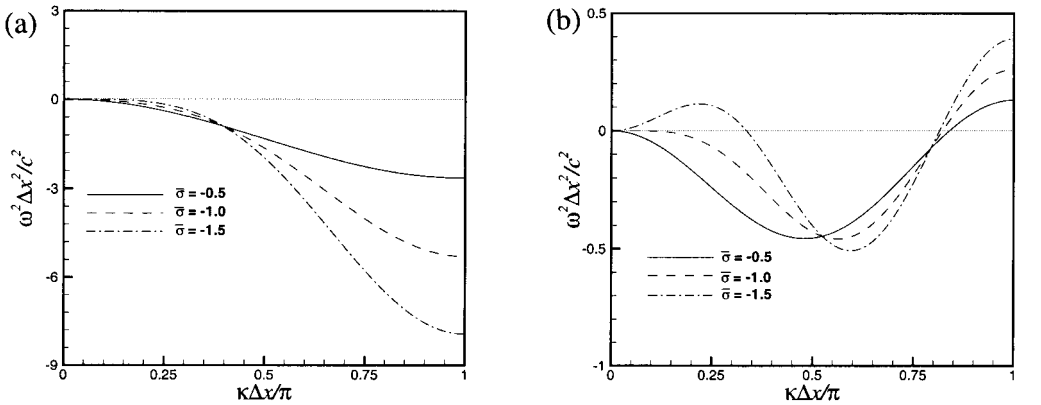

Figure 4. Frequency–wave number relations in plane wave by EFG with nodal integration and Eulerian kernel $c^2 = -C^{\sigma\mathscr{J}}/\rho$: (a) $D_{\mathrm{mx}} = 1.5$; and (b) $D_{\mathrm{mx}} = 2.5$.

4.1.2. Lagrangian kernel. For the Lagrangian kernel, the internal nodal force is given by (53), which simplifies in one dimension to

$$f_I^{\mathrm{int}} = \int_{\Omega_0} \phi_I'(X) P(X)\, \mathrm{d}\Omega \tag{77}$$

The deformation gradient is computed by

$$F(X) = 1 + \frac{\partial u}{\partial X} = 1 + \sum_J \phi_J'(X) u_J \tag{78}$$

With nodal quadrature of (77), the internal nodal force is given by

$$f_I^{\mathrm{int}} = \sum_J V_J^0 \phi_I'(X_J) P_J \tag{79}$$

This can also be obtained from (64) and (66). The perturbed momentum equation is

$$m_I \ddot{\tilde{u}}_I = -\sum_J V_J^0 \phi_I'(X_J) \tilde{P}_J \tag{80}$$

where

$$\tilde{P}_I = \bar{C}_I^{\mathrm{SE}} \tilde{F}_I, \quad \bar{C}_I^{\mathrm{SE}} = (C^{\mathrm{SE}} F^2 + S)|_I, \quad \tilde{F}_I = \sum_J \phi_J'(X_I) \tilde{u}_J \tag{81}$$

For identical, uniformly spaced nodes and a symmetric weight function, the dispersion equation is as follows:

$$\omega^2 = \frac{\bar{C}^{\mathrm{SE}}}{\rho_0} \left[\sum_j \phi'(j\Delta X) \sin(\kappa j \Delta X) \right]^2 \tag{82}$$

By comparing the above with (74), it can be seen that the particle equations with a Lagrangian kernel *do not exhibit the tensile instability* regardless of the magnitude of the tensile stress. This favourable property arises from *the use of a Lagrangian kernel* $W(\mathbf{X})$. Comparing the above

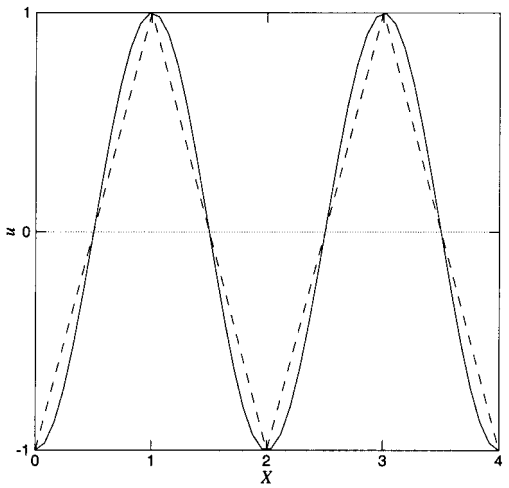

Figure 5. Spurious mode in one-dimensional discrete equation with nodal integration (dashed line corresponds to cuf-off frequency for linear-displacement finite elements).

with Equation (32), shows that the unstable behaviour of the Lagrangian kernel is much closer to the continuum behaviour, Equation (32), than the Eulerian kernel, Equation (74). As in the continuum, instabilities occur for the Lagrangian kernel when $\bar{C}^{\mathrm{SE}} \leqslant 0$. However, in the Eulerian kernel according to Equation (74), the tensile instability occurs due to the second and third terms of that equation; these terms are absent in the Lagrangian kernel, Equation (82), and in the continuum, Equation (32). Note that for small κ, the RHS in Equations (32) and (82) are approximately equal.

The Lagrangian kernel does not eliminate the instability due to rank deficiency. From the dispersion Equation (82), we see that $\omega = 0$ for wave number $\kappa = \pi/\Delta X$, which is the cut-off wave number for a uniform nodal spacing ΔX. This implies the existence of a spurious mode in the discrete equation due to rank deficiency; the mode is the same as with the Eulerian kernel, which is shown in Figure 5.

We consider a simple example to check the tensile instability in Eulerian and Lagrangian kernels. A rod is fixed at both ends and with an initial stress ($\sigma_0 = 1.0\,\mathrm{GPa}$). The centre node was given an initial velocity ($v_0 = 40\,\mathrm{m/s}$). EFG with nodal integration is used with Eulerian and Lagrangian kernels. The material constants are $\rho = 2450\,\mathrm{kg/m^3}$, $E = 10.0\,\mathrm{GPa}$, $l = 0.04\,\mathrm{m}$.

The velocity at the centre node is shown in Figure 6. From Figure 6, we see that the tensile instability will occur for the Eulerian kernel but not the Lagrangian kernel (note the velocity for the Eulerian kernel is 10 times larger). Figure 7 shows the displacement near the centre of rod which also shows evidence of an instability for the Eulerian kernel. However, for the Lagrangian kernel (Figure 6(b)) no tensile instability occurs.

4.2. Stress point integration in plane wave

4.2.1. Eulerian kernel. In one dimension, for uniformly placed particles, we place stress points at the centre of each interval (see Figure 8). With stress point integration, the internal nodal force,

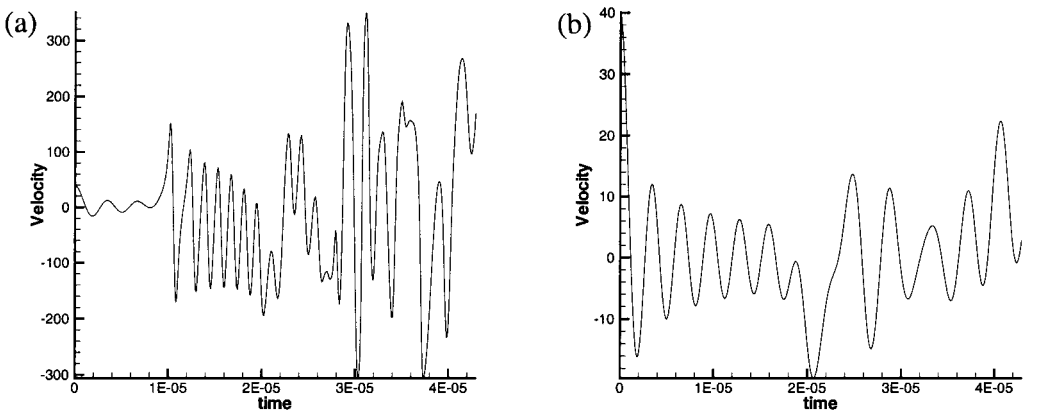

Figure 6. Stability comparing by EFG nodal integration in the rod with initial stress when $D_{\mathrm{mx}} = 1.5$: (a) Eulerian kernel; and (b) Lagrangian kernel.

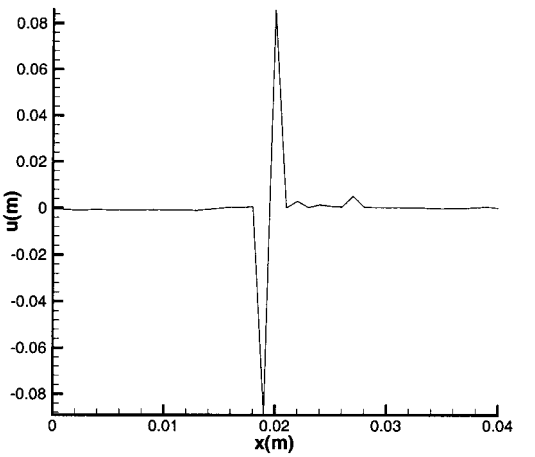

Figure 7. Displacement distribution along the rod when using Eulerian kernel at $t = 4.3 \times 10^{-5}$ s ($D_{\mathrm{mx}} = 1.5$).

Equation (65), is given by

$$f_I^{\mathrm{int}} = \sum_{J \in \mathcal{N}_M} V_J^M \phi_I'(x_J^M)\sigma_J^M + \sum_{J \in \mathcal{N}_S} V_J^S \phi_I'(x_J^S)\sigma_J^S \tag{83}$$

where $\mathcal{N}_M$, $\mathcal{N}_S$ are the sets of master and stress points contributing to the integral. V_J^M and V_J^S are current volumes for the master nodes and stress points. These volumes differ from the volumes associated with m_J in the inertial term; in this one-dimensional case,

$$V_J^M = V_J^S = V_J/2 = \frac{m_J F_J}{2\rho_{0J}} \tag{84}$$

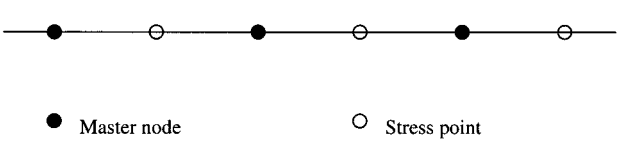

Figure 8. Stress points in one dimension.

The deformation gradient is computed from the displacements of the supporting master nodes at both master nodes and stress points,

$$F_I = \frac{1}{1 - \left.\dfrac{\partial u}{\partial x}\right|_I}, \quad \left.\frac{\partial u}{\partial x}\right|_I = \sum_{J \in \mathcal{N}_M} \phi'_J(x_I) u_J^M \quad \text{for } x_I = x_I^M \text{ or } x_I^S \tag{85}$$

The perturbed momentum equation is

$$\begin{aligned} m_I \ddot{\tilde{u}}_I = &- \sum_{J \in \mathcal{N}_M} \frac{m_J}{2\rho_{0J}} \left[\phi'_I(x_J^M)(\tilde{\sigma}_J^M F_J^M + \sigma_J^M \tilde{F}_J^M) + \tilde{\phi}'_I(x_J^M)\sigma_J^M F_J^M \right] \\ &- \sum_{J \in \mathcal{N}_S} \frac{m_J}{2\rho_{0J}} \left[\phi'_I(x_J^S)(\tilde{\sigma}_J^S F_J^S + \sigma_J^S \tilde{F}_J^S) + \tilde{\phi}'_I(x_J^S)\sigma_J^S F_J^S \right] \end{aligned} \tag{86}$$

where from (64)

$$\tilde{\sigma}_J = \tilde{P}_J = \bar{C}_J^{\sigma\mathscr{T}} F^{-1} \tilde{F}_J \tag{87}$$

$$\tilde{F}_J = \left.\frac{\partial \tilde{u}}{\partial X}\right|_J = F_J \sum_{K \in \mathcal{N}_M} \phi'_K(x_J) \tilde{u}_K^M \quad \text{for } x_J = x_J^M \text{ or } x_J^S \tag{88}$$

$$\tilde{\phi}'_I(x_J) = \phi''_I(x_J)(\tilde{u}_J - \tilde{u}_I^M) \quad \text{for } \tilde{u}_J = \tilde{u}_J^M \text{ or } \tilde{u}_J^S \tag{89}$$

Since the displacement at a stress point is determined by its neighbouring master nodes,

$$u_J^S = \sum_{K \in \mathcal{N}_M} \phi_K(x_J^S) u_K^M \tag{90}$$

then

$$\tilde{u}_J^S = F_J^S \sum_{K \in \mathcal{N}_M} [\phi_K(x_J^S) - \phi'_K(x_J^S) u_K^M] \tilde{u}_K^M \tag{91}$$

Note that F is constant and the current distance between nodes, Δx, is uniform. Therefore, if we assume the displacement at node I vanishes, we have

$$u_K^M = \frac{F-1}{F}(K - I)\Delta x \tag{92}$$

For a symmetric weight function and identical particles, we have the following dispersion equation:

$$\omega^2 = \frac{\bar{C}^{\sigma\mathscr{T}}}{2\rho}\left\{\left[\sum_j \phi'_M(j)s_M(j)\right]^2 + \left[\sum_j \phi'_S(j)s_S(j)\right]^2\right\}$$
$$-\frac{\sigma}{2\rho}\left\{\sum_j \phi''_M(j)[1-c_M(j)] - \left[\sum_j \phi'_M(j)s_M(j)\right]^2\right.$$
$$+\sum_j \phi''_S(j) - \left[\sum_j \phi'_S(j)s_S(j)\right]^2$$
$$-F\sum_j \phi''_S(j)c_S(j)\sum_j \phi_S(j)c_S(j)$$
$$+(F-1)\Delta x\sum_j \phi''_S(j)c_S(j)\sum_j \left(j+\frac{1}{2}\right)\phi'_S(j)c_S(j)$$
$$\left.+(F-1)\Delta x\sum_j \left(j+\frac{1}{2}\right)\phi''_S(j)s_S(j)\sum_j \phi'_S(j)s_S(j)\right\} \tag{93}$$

where

$$s_M(j) = \sin(\kappa j\Delta x), \quad s_S(j) = \sin(\kappa(j+\tfrac{1}{2})\Delta x) \tag{94}$$

$$c_M(j) = \cos(\kappa j\Delta x), \quad c_S(j) = \cos(\kappa(j+\tfrac{1}{2})\Delta x) \tag{95}$$

$$\phi''_M(j) = \phi''(j\Delta x), \quad \phi''_S(j) = \phi''((j+\tfrac{1}{2})\Delta x) \tag{96}$$

$$\phi'_M(j) = \phi'(j\Delta x), \quad \phi'_S(j) = \phi'((j+\tfrac{1}{2})\Delta x) \tag{97}$$

$$\phi_S(j) = \phi((j+\tfrac{1}{2})\Delta x) \tag{98}$$

Figure 9 shows the frequency–wave number relations as a function of stress levels ($\bar{\sigma} = \sigma/C^{\sigma\mathscr{T}}$) for different values of D_{mx}, where $c^2 = C^{\sigma\mathscr{T}}/\rho$. The quartic spline is used as the weight function. For small support, there is no tensile instability. However, when the support size is increased, e.g. $D_{\mathrm{mx}} = 2.5$, an instability occurs at the cut off wave number for $\bar{\sigma} = 1$.

4.2.2. Lagrangian kernel. For a Lagrangian kernel with stress point integration, the internal nodal force, Equation (77), is

$$f_I^{\mathrm{int}} = \sum_{J\in\mathscr{N}_M} V_J^{0M}\phi'_I(X_J^M)P_J^M + \sum_{J\in\mathscr{N}_S} V_J^{0S}\phi'_I(X_J^S)P_J^S \tag{99}$$

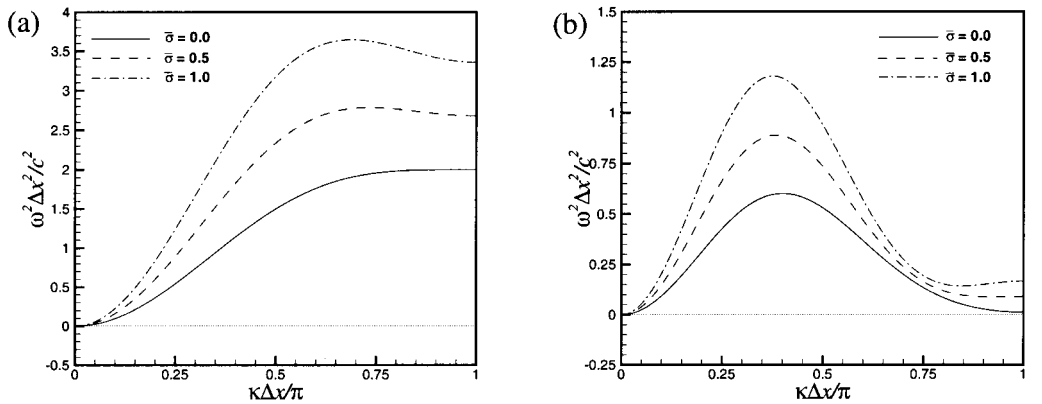

Figure 9. Frequency–wave number relations in plane wave by EFG with stress point integration and Eulerian kernel: (a) $D_{\mathrm{mx}} = 1.5$; and (b) $D_{\mathrm{mx}} = 2.5$.

where $\mathcal{N}_M$, $\mathcal{N}_S$ are the sets of master and stress points contributing to the integral. Thus, the perturbed momentum equation is

$$m_I \ddot{\tilde{u}}_I = -\sum_{J\in\mathcal{N}_M} V_J^{0M}\tilde{P}_J^M \phi'(X_J^M - X_I^M) - \sum_{J\in\mathcal{N}_S} V_J^{0S}\tilde{P}_J^S \phi'(X_J^S - X_I^M) \tag{100}$$

Note that the volume V^{0M} is different from V^0 for the master nodes; in this one-dimensional case, $V^{0M} = V^{0S} = V^0/2$. The stresses are calculated from the displacements of supporting master nodes by

$$\tilde{P}_J^M = \bar{C}_J^{\mathrm{SE}}\tilde{F}_J^M = \bar{C}_J^{\mathrm{SE}} \sum_K \phi'(X_J^M - X_K^M)\tilde{u}_K \tag{101}$$

$$\tilde{P}_J^S = \bar{C}_J^{\mathrm{SE}}\tilde{F}_J^S = \bar{C}_J^{\mathrm{SE}} \sum_K \phi'(X_J^S - X_K^M)\tilde{u}_K \tag{102}$$

By similar algebra we obtain the following dispersion equation:

$$\omega^2 = \frac{\bar{C}^{\mathrm{SE}}}{2\rho_0}\left\{\left[\sum_j \phi'(j\Delta X)\sin(\kappa j\Delta X)\right]^2 + \left[\sum_j \phi'\left(\left(j+\frac{1}{2}\right)\Delta X\right)\sin\left(\kappa\left(j+\frac{1}{2}\right)\Delta X\right)\right]^2\right\} \tag{103}$$

With a Lagrangian kernel and stress point integration, the tensile instability is eliminated. The frequency relations based on the above dispersion equation are shown in Figure 10 for various smoothing lengths ($h = D_{\mathrm{mx}}\Delta X$) and a cubic spline weight function. It can be seen that there are no unstable modes due to rank deficiency. However, the frequency is very small near the cut-off point for large dilation ($D_{\mathrm{mx}} \geqslant 3.0$). This indicates the stiffness matrix is nearly singular for large support.

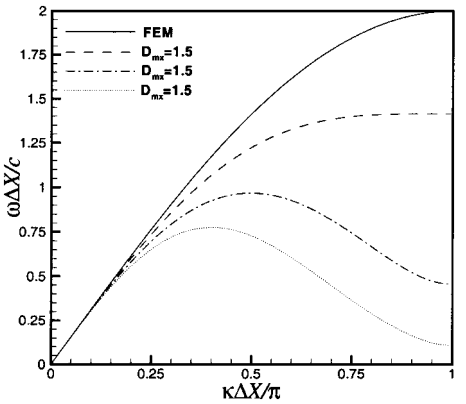

Figure 10. Frequency relations in plane wave by EFG with stress points and Lagrangian kernel with $c^2 = \bar{C}^{\mathrm{SE}}/\rho_0$.

For comparison, the dispersion relation for the two-node linear displacement finite element with lumped mass is also given in this figure. It can be seen that the frequency given by the EFG and SPH methods is lower than that of FEM, especially for large wave numbers, so the high-frequency accuracy of particle methods is less than that of FEM. In EFG with background quadrature, the frequency errors are reduced.

4.3. Least-squares stabilization

To stabilize nodal integration of EFG, Beissel and Belytschko [2] proposed a stabilization term which contains the square of the residual of the momentum equation. In the following we study the stability of this method.

The weak form for this stabilization in one dimension is

$$\int_\Omega \delta u(\rho\ddot{u} - \sigma_{,x} - \rho b)\,\mathrm{d}\Omega + \frac{\beta}{E}\int_\Omega \delta\sigma_{,x}(\sigma_{,x} + \rho b - \rho\ddot{u})\,\mathrm{d}\Omega = 0 \tag{104}$$

In the above E is the Young's modulus and $\beta = \alpha_{\mathrm{s}} l_{\mathrm{c}}^2$, where l_{c} is a characteristic length of the discretization and α_{s} is a dimensionless stabilization parameter. The discrete equation can be written as

$$\sum_K M_{IK}\ddot{u}_K = f_I^{\mathrm{ext}} - \sum_K K_{IK}u_K \tag{105}$$

where the mass and stiffness matrices are computed by nodal integration

$$M_{IK} = \sum_J \rho V_J \phi_I(x_J)\phi_K(x_J) - \beta\sum_J \rho V_J \phi_I''(x_J)\phi_K(x_J) \tag{106}$$

$$K_{IK} = \sum_J EV_J \phi_I'(x_J)\phi_K'(x_J) + \beta\sum_J EV_J \phi_I''(x_J)\phi_K''(x_J) \tag{107}$$

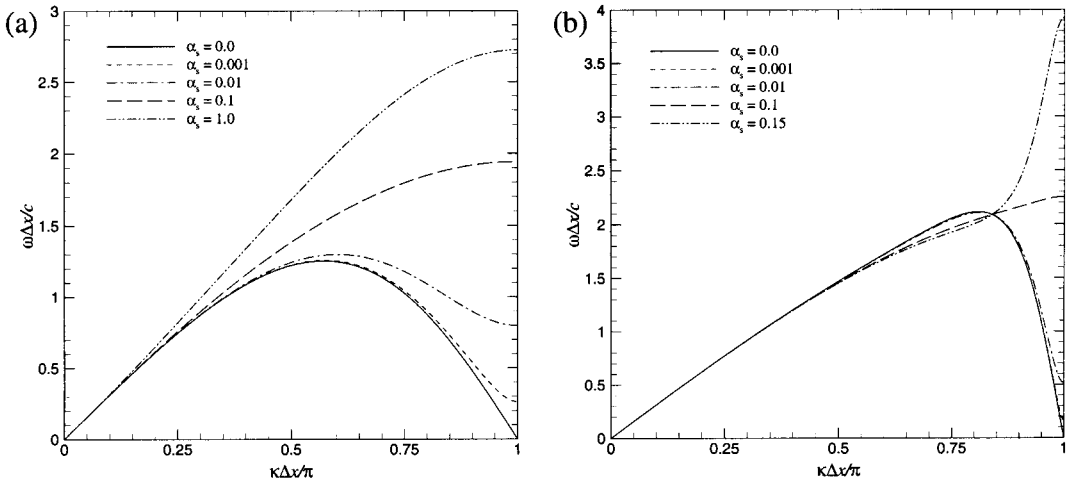

Figure 11. Frequency–wave number relations in plane wave with Beissel–Belytschko-stabilized EFG nodal integration: (a) $D_{\mathrm{mx}} = 1.5$; and (b) $D_{\mathrm{mx}} = 2.5$.

We assume the nodes are identical and uniformly spaced, and the weight function is symmetric. For the perturbation, Equation (69), the dispersion equation is

$$\left(\frac{\omega}{c}\right)^2 = \left\{ \left[\sum_j \phi'(j\Delta x)\sin(\kappa j\Delta x)\right]^2 + \beta\left[\sum_j \phi''(j\Delta x)\cos(\kappa j\Delta x)\right]^2 \right\} \Bigg/ \left\{ \left[\sum_j \phi(j\Delta x)\cos(\kappa j\Delta x)\right]^2 - \beta\sum_j \phi''(j\Delta x)\cos(\kappa j\Delta x)\sum_j \phi(j\Delta x)\cos(\kappa j\Delta x) \right\} \tag{108}$$

where $c = \sqrt{E/\rho}$.

Figure 11 shows the frequency as a function of the relative wave number for $\sigma = 0$, where $\alpha_s = 0.0$ corresponds to unstabilized nodal integration. For small dilations, the addition of the stabilization terms removes the spurious mode due to rank deficiency. With the increase of the stabilization parameter, the frequency decreases less near the cut-off point. For dilation $D_{\mathrm{mx}} \geqslant 2.5$, the stability property of the Beissel–Belytschko method changes. If stabilization parameter is small ($\alpha_s = 0.001$) the improvement in the stability is not significant. On the other hand, if the stabilization parameter is too large, ω will vanish or become imaginary for certain wave numbers, indicating an instability. The reason for this is that with $D_{\mathrm{mx}} = 2.5$, the stabilization term in the mass (the second term in the denominator in Equation (108)) will change to positive for large wave numbers, causing the denominator to be zero or negative. Thus, the method's effectiveness diminishes for moderate and large dilations.

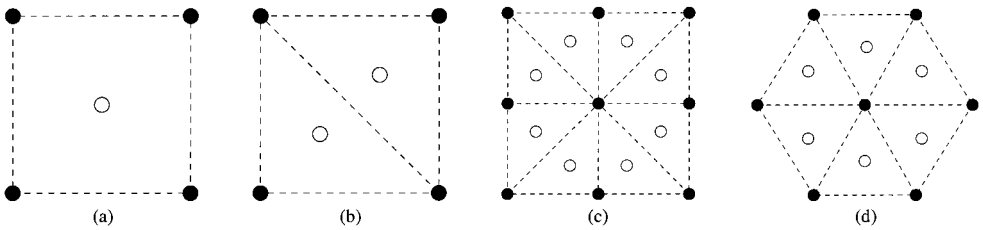

Figure 12. Initial position of stress point: (a) center of quadrilateral; (b) center of triangle; (c) star shape; and (d) hexagonal shape.

4.4. Two-dimensional anti-plane wave

To investigate stability in higher dimensions, we consider a two-dimensional anti-plane motion in an infinite slab:

$$v_z(x,\ y) \neq 0, \quad v_x = v_y = 0 \tag{109}$$

For the sake of simplicity, we consider uniformly spaced particles. Our focus is on the relationship between the placement of the stress points and instability due to rank deficiency. The following patterns are considered (see Figure 12 where the filled circles indicate master nodes and the empty circles denote stress points):

(i) Connect every four master particles to form a virtual quadrilateral and place one stress point at the centre of the quadrilateral.
(ii) Divide each quadrilateral formed in method (a) into two virtual triangles and place one stress point at the centre of the triangle.
(iii) Stress points at the centres of virtual triangles in a star-shape pattern.
(iv) Stress points at the centres of virtual triangles in a hexagonal pattern.

Among the methods suggested above, method (a) will add the fewest number of stress points in a mesh.

The linearized momentum equation in the absence of initial stress is

$$\ddot{u} = c^2 \Delta u = c^2 \left(\frac{\partial^2 u}{\partial x^2} + \frac{\partial^2 u}{\partial y^2} \right) \tag{110}$$

where $c = \sqrt{G^{\tan}/\rho}$ is the wave speed and $G^{\tan}$, ρ are, respectively, the tangent shear modulus and density. The discrete momentum equation is

$$M_{IJ} \ddot{u}_J = -c^2 K_{IJ} u_J \tag{111}$$

where repeated indices are summed over the appropriate range and

$$M_{IJ} = \int_\Omega \phi_I \phi_J \, \mathrm{d}\Omega \tag{112}$$

$$K_{IJ} = \int_\Omega (\phi_{I,x} \phi_{J,x} + \phi_{I,y} \phi_{J,y}) \, \mathrm{d}\Omega \tag{113}$$

If the master nodal spacings in the x- and y-direction are Δx and $\Delta y = \gamma \Delta x$, the spatial coordinates of a particle can be expressed as $(j\Delta x, k\Delta y)$ and the perturbation at this point is denoted by $u_{j,k} = u(j\Delta x, k\Delta y)$. Then, at an interior particle $(m\Delta x, n\Delta y)$, Equation (111) can be rewritten in terms of the relative spatial intervals from this interior point as

$$M_{jk}\ddot{u}_{m+j,n+k} = -c^2 K_{jk} u_{m+j,n+k} \tag{114}$$

Consider a plane wave perturbation

$$u_{m,n} = A \exp[\mathrm{i}\kappa(m\Delta x \cos\theta + n\Delta y \sin\theta) - \mathrm{i}\omega t] \tag{115}$$

where κ is the wave number, ω is the circular frequency, θ is the angle of the normal direction of the wavefront, and $\mathrm{i} = \sqrt{-1}$. Substituting (115) into the discrete equation (114) yields

$$\omega^2 M_{jk} E_{jk} = c^2 K_{jk} E_{jk} \tag{116}$$

where

$$E_{jk} = \exp[\mathrm{i}\kappa(j\Delta x \cos\theta + k\Delta y \sin\theta)] = \exp[\mathrm{i}\kappa\Delta x(j\cos\theta + k\gamma \sin\theta)] \tag{117}$$

The matrices M_{jk} and K_{jk} have symmetries about this evaluation point. The normalized frequency is given by

$$\frac{\omega\Delta x}{c} = \left\{ \frac{K_{jk}\cos[\kappa\Delta x(j\cos\theta + k\gamma\sin\theta)]}{M_{jk}\cos[\kappa\Delta x(j\cos\theta + k\gamma\sin\theta)]/\Delta x^2} \right\}^{1/2} \tag{118}$$

If the lumped mass is used, $M = \Delta x \Delta y = \gamma \Delta x^2$, and the frequency is

$$\frac{\omega\Delta x}{c} = \left\{ \frac{1}{\gamma} K_{jk}\cos[\kappa\Delta x(j\cos\theta + k\gamma\sin\theta)] \right\}^{1/2} \tag{119}$$

The numerical values of the stiffness matrix for various implementations of meshfree method are listed in Table I. The parameter for the domain of support, $D_{\mathrm{mx}} = 2.0$ and $\gamma = \Delta x/\Delta y = 1.0$. The entries for $(\pm j, \pm k)$ include four combinations, (j, k), $(j, -k)$, $(-j, k)$, and $(-j, -k)$. The plots for the frequency as a function of relative wave number for various propagation directions are shown in Figures 13–15.

For a set of particles uniformly distributed in the x- and y-direction, the maximum admissible wave number is $\kappa = \pi/\Delta x$ for $\theta = 0^\circ$ and $\kappa = \sqrt{2}\pi/\Delta x$ for $\theta = 45^\circ$. With nodal integration, the frequencies at these cut-off points vanish (see Figure 13), indicating the presence of instability due to rank deficiency in the discrete equations. The two associated spurious modes are shown in Figure 16. It can be seen that the spurious mode at $\theta = 45^\circ$ is similar to the hourglass mode in finite elements [36].

For cell integration and stress point integration, the spurious mode occurs only at $\theta = 45^\circ$ for background cell integration with one quadrature point or stress point integration with stress points at the centre of quadrilateral (see Figures 14(a) and 15(a)).

Stress points at the centre of the quadrilateral cannot eliminate the spurious mode. This can be deduced from the previous results. In one-point cell quadrature, if the cells are generated by the nodes, the quadrature point coincides with the stress point. Thus, stress point quadrature is equivalent to the superposition of nodal integration and one-point cell integration. Because neither integration scheme eliminates the spurious mode for $\theta = 45^\circ$, stress point integration cannot

Table I. Values of stiffness matrix K_{jk} for various implementations.

j	k	Nodal integration	Cell integration 2×2	Cell integration one point	Stress point quadrilateral
0	0	0.5062	0.6507	0.8142	0.6602
±1	0	0.1101	0.1016	0.9911×10^{-1}	0.1046
0	±1	0.1101	0.1016	0.9911×10^{-1}	0.1046
±1	±1		-0.5933×10^{-1}	-0.1456	-0.7282×10^{-1}
±2	0	-0.1132	-0.8733×10^{-1}	-0.4677×10^{-1}	-0.7997×10^{-1}
0	±2	-0.1132	-0.8733×10^{-1}	-0.4677×10^{-1}	-0.7997×10^{-1}
±2	±1	-0.5504×10^{-1}	-0.5223×10^{-1}	-0.4677×10^{-1}	-0.5090×10^{-1}
±1	±2	-0.5504×10^{-1}	-0.5223×10^{-1}	-0.4677×10^{-1}	-0.5090×10^{-1}
±2	±2	-0.1338×10^{-1}	-0.8851×10^{-2}	-0.4173×10^{-2}	-0.8778×10^{-2}
±3	0		-0.2663×10^{-2}	-0.5564×10^{-2}	-0.2782×10^{-2}
0	±3		-0.2663×10^{-2}	-0.5564×10^{-2}	-0.2782×10^{-2}
±3	±1		-0.8141×10^{-3}	-0.3478×10^{-2}	-0.1739×10^{-2}
±1	±3		-0.8141×10^{-3}	-0.3478×10^{-2}	-0.1739×10^{-2}
±3	±2			-0.9193×10^{-5}	
±2	±3			-0.9193×10^{-5}	

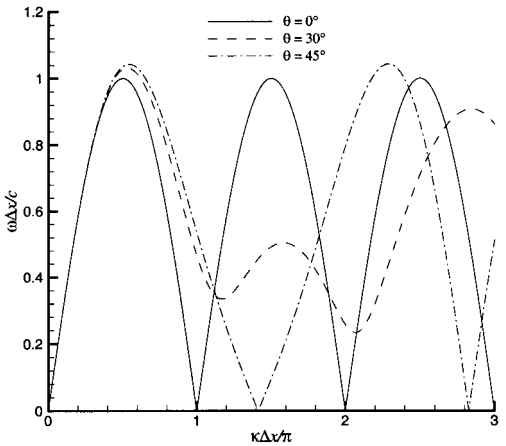

Figure 13. Frequency–wave number relations in anti-plane wave with EFG nodal integration.

eliminate the mode either. Based on this reasoning, if we move the position of the stress point from the centre, e.g. place the stress point randomly inside the virtual quadrilateral, the spurious modes can be suppressed. However, this approach is generally not practical: unless the stress particle is far from the centre of the quadrilateral, the discrete equations will be nearly singular.

As shown in Figures 15(b) and 15(c), the stability of the star-shaped pattern is almost identical to that with the stress points located at the centre of virtual triangle generated on a rectangular grid of nodes. However, with the star-shaped pattern the mesh is symmetric and the stiffness matrix is symmetric about the evaluation point. For the hexagonal pattern, Figure 15(d), there are no spurious modes. The frequency–wave number relations for $\theta = 0$ and 90° differ since the nodal

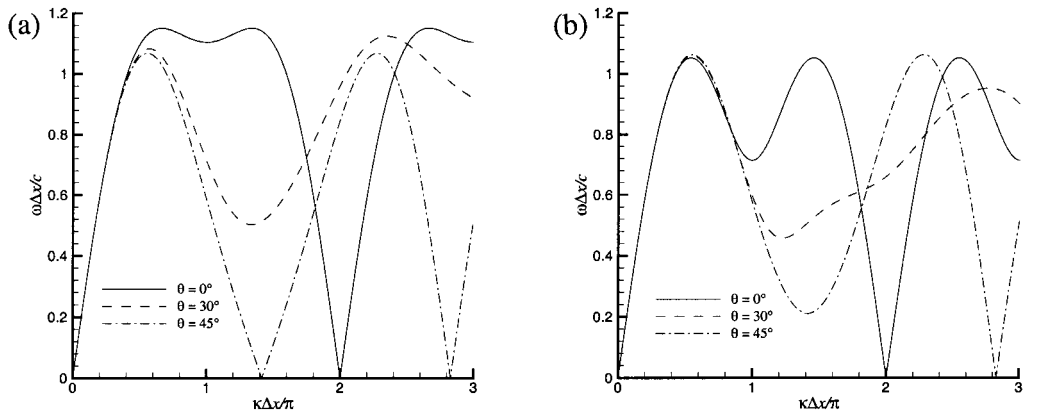

Figure 14. Frequency-wave number relations in anti-plane wave with EFG cell integration: (a) one-point cell quadrature; and (b) 2×2 cell quadrature.

distributions differ in the x- and y-direction. It can also be seen that the drop in the frequency near the cut-off point is less than for other cases, so the higher frequencies will be more accurate. This indicates that hexagonal arrangements of particles with stress points within each virtual triangle are best from the viewpoints of accuracy and stability due to rank deficiency.

5. STABLE TIME STEP FOR MESHLESS METHODS

The stable critical time step for central difference integration can be obtained from the maximum frequencies based on the dispersion relations using (see e.g. [29])

$$\Delta t^{\text{crit}} = \max_i \frac{2}{\omega_i}(\sqrt{\xi_i^2 + 1} - \xi_i) \tag{120}$$

where ω_i is the frequency and ξ_i the fraction of critical damping in this mode.

For non-uniform arrangements of the particles, the critical time step can be obtained by the eigenvalue inequality. This theorem states that if

$$\mathbf{K} = \sum_{e=1}^{N_e} \mathbf{K}_e = \sum_{e=1}^{N_e} \sum_{Q=1}^{N_Q} \mathbf{K}_e^Q \tag{121}$$

$$\mathbf{M} = \sum_{e=1}^{N_e} \mathbf{M}_e = \sum_{e=1}^{N_e} \sum_{Q=1}^{N_Q} \mathbf{M}_e^Q \tag{122}$$

where N_e is the number of elements or cells, N_Q is the number of quadrature points in each cell or element, $\mathbf{K}_e^Q$ and $\mathbf{M}_e^Q$ are the stiffness and mass matrices at quadrature point Q in cell e, then

$$\min_e \left(\min_Q \lambda_{\min}^Q \right) \leqslant \lambda_{\min}^G \leqslant \lambda_{\max}^G \leqslant \max_e \left(\max_Q \lambda_{\max}^Q \right) \tag{123}$$

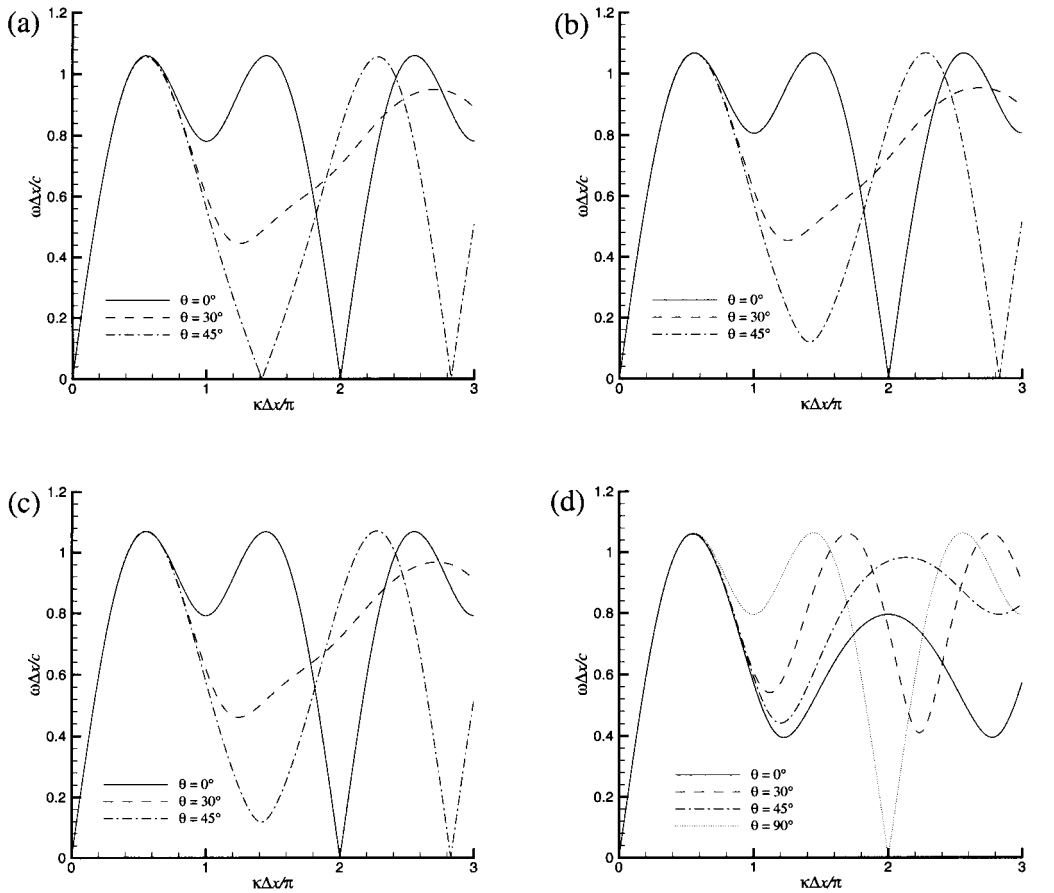

Figure 15. Frequency–wave number relations for anti-plane wave with EFG stress point integration and SPH with stress points: (a) stress point at centre of quadrilateral; (b) stress point at centre of triangle; (c) star-shaped pattern; and (d) hexagonal pattern.

where $\lambda^Q_{\min}$, $\lambda^Q_{\max}$ are the minimum and maximum eigenvalues at quadrature point Q and $\lambda^G_{\min}$, $\lambda^G_{\max}$ are the extremal eigenvalues of the assembled system. Therefore, a conservative estimate of the critical time step for the central difference method is

$$\Delta t^{\text{crit}} = \frac{2}{\omega^G_{\max}} = \frac{2}{\sqrt{\lambda^G_{\max}}} = \min_e \frac{2}{(\max_Q \lambda^Q_{\max})^{1/2}} \tag{124}$$

5.1. *Maximum eigenvalue bound of one-dimensional EFG*

In any quadrature scheme, the stiffness and mass matrices in one dimension are

$$\mathbf{K} = \sum_Q \mathbf{K}(x_Q) = \sum_Q \mathbf{K}^Q, \quad \mathbf{M} = \sum_Q \mathbf{M}(x_Q) = \sum_Q \mathbf{M}^Q \tag{125}$$

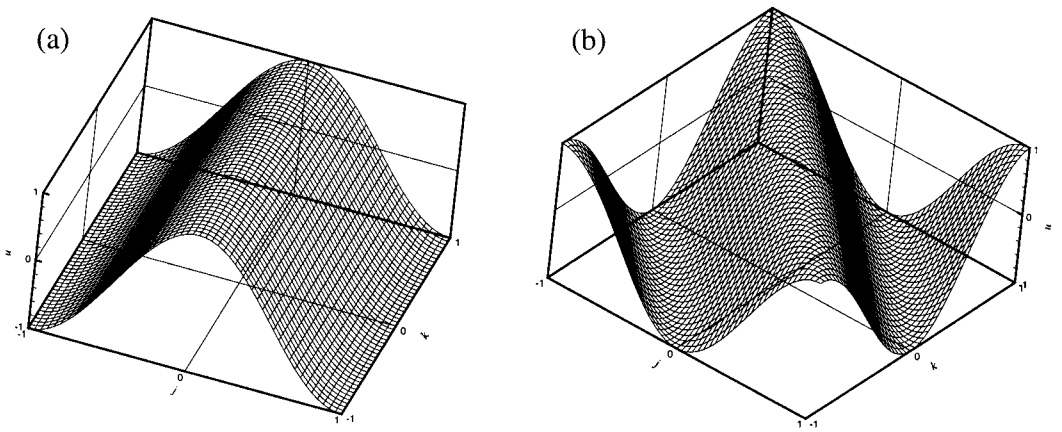

Figure 16. Spurious modes in the discrete wave equation: (a) $\kappa\Delta x = \pi$ at $\theta = 0°$; and (b) $\kappa\Delta x = \sqrt{2}\pi$ at $\theta = 45°$.

where

$$\mathbf{K}^{Q} = w_Q EJ \boldsymbol{\Phi}_{,x}^{\mathrm{T}}(x_Q)\boldsymbol{\Phi}_{,x}(x_Q) \tag{126}$$

$$\mathbf{M}^{Q} = w_Q \rho J \boldsymbol{\Phi}^{\mathrm{T}}(x_Q)\boldsymbol{\Phi}(x_Q), \quad J = \frac{h_{\mathrm{c}}}{2} \tag{127}$$

In the above x_Q, w_Q are the co-ordinate and the weight of the quadrature point, respectively, and h_{c} is the length of the cell. Since $\boldsymbol{\Phi}_{,x}$ is a vector, $\mathbf{K}^{Q}$ is a matrix of rank 1 at most. Therefore, the following eigenproblem has at most one non-zero eigenvalue,

$$\mathbf{K}^{Q}\mathbf{v}^{Q} - \lambda^{Q}\mathbf{M}^{Q}\mathbf{v}^{Q} = 0 \tag{128}$$

Writing out (126) and (127) gives

$$\mathbf{K}^{Q} = w_Q EJ \begin{bmatrix} \phi_{1,x}\phi_{1,x} & \phi_{1,x}\phi_{2,x} & \cdots & \phi_{1,x}\phi_{N,x} \\ \phi_{2,x}\phi_{1,x} & \phi_{2,x}\phi_{2,x} & \cdots & \phi_{2,x}\phi_{N,x} \\ \vdots & \vdots & & \vdots \\ \phi_{N,x}\phi_{1,x} & \phi_{N,x}\phi_{2,x} & \cdots & \phi_{N,x}\phi_{N,x} \end{bmatrix} \tag{129}$$

$$\mathbf{M}^{Q} = w_Q \rho J \begin{bmatrix} \phi_1\phi_1 & \phi_1\phi_2 & \cdots & \phi_1\phi_N \\ \phi_2\phi_1 & \phi_2\phi_2 & \cdots & \phi_2\phi_N \\ \vdots & \vdots & & \vdots \\ \phi_N\phi_1 & \phi_N\phi_2 & \cdots & \phi_N\phi_N \end{bmatrix} \tag{130}$$

where ϕ_I, $I=1$ to N, are the shape functions which are non-zero at x_Q. If the mass matrix is diagonalized by the row sum technique, the lumped mass matrix is

$$\mathbf{M}^Q_{\text{lump}} = w_Q \rho J \begin{bmatrix} \phi_1 & & & \\ & \phi_2 & & \\ & & \ddots & \\ & & & \phi_N \end{bmatrix} \tag{131}$$

Obviously, the only non-zero eigenvalue of (128) with the above lumped mass is

$$\lambda^Q = c^2 \sum_{I=1}^{N} \frac{\phi^2_{I,x}(x_Q)}{\phi_I(x_Q)} \tag{132}$$

and the corresponding eigenvector is

$$\mathbf{v}^Q = \begin{bmatrix} \dfrac{\phi_{1,x}}{\phi_1} & \dfrac{\phi_{2,x}}{\phi_2} & \cdots & \dfrac{\phi_{N,x}}{\phi_N} \end{bmatrix}^{\mathrm{T}}_{x_Q} \tag{133}$$

where c is the wave velocity, $c=\sqrt{E/\rho}$.

For uniformly spaced particle, the shape functions can be expressed in terms of the weight as [37]

$$\phi_I(x) = \Delta x W_I(x) \tag{134}$$

Note that the above holds for both SPH and an approximation based on MLS, such as EFG, since the SPH does not require a correction for linear completeness for uniformly spaced particles in the absence of a boundary. The derivative is then given by

$$\phi_{I,x}(x) + \Delta x W_{I,x}(x) \tag{135}$$

For uniformly distributed particles, we have

$$\lambda^Q \leqslant c^2 \frac{N}{2} \frac{0.2587 \times 48 \Delta x}{h^3}$$

where h is the size of the support. Since $N \approx 2h/\Delta x$, we finally have

$$\lambda^Q \leqslant \alpha \frac{c^2}{h^2}, \quad \alpha = 12.42 \tag{136}$$

By the generalized element eigenvalue inequality, the above is an upper bound on the maximum eigenvalue of the system, i.e.

$$\lambda^G_{\max} \leqslant \max_{\text{cell}} \left(\max_Q \lambda^Q \right) \leqslant \alpha \frac{c^2}{h^2} \tag{137}$$

Since the support h is determined by the dilation parameter ($h = D_{\max} \Delta x$), the upper bound in the above changes with support size for a given arrangement of particles. By comparison, the corresponding maximum eigenvalue for linear displacement finite elements is

$$\lambda^{\text{FEM}}_{\max} = \frac{4c^2}{\Delta x^2} \tag{138}$$

Table II. Maximum eigenvalues for uniformly spaced particles based on Fourier analysis.

Particle method	Normalized $\lambda_{\max}$
Nodal integration with both kernels	1.0
Stress points with Eulerian kernel	4.0
Stress points with Lagrangian kernel	2.0

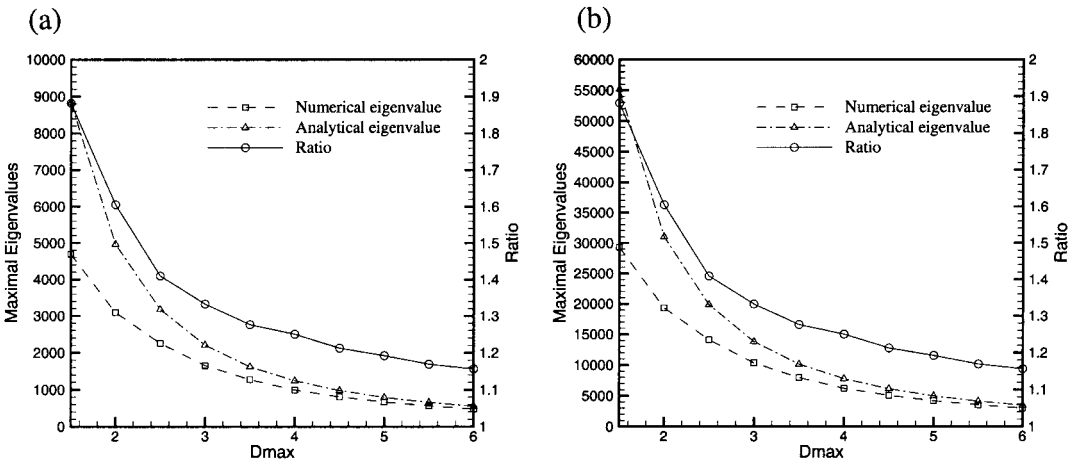

Figure 17. Maximal eigenvalues of a one-dimensional bar with EFG: (a) number of nodes: 41; and (b) number of nodes: 101.

Also from the Fourier analysis in the previous section, we have maximum eigenvalues for some particle discretizations with uniformly spaced particles; see Table II where the initial stress is zero, $D_{\mathrm{mx}} = 1.5$ and the maximum eigenvalues are normalized by $c^2/\Delta x^2$ or $c^2/\Delta X^2$. To compare this result with an exact eigenvalue, we discretize a bar with length of 1 by 41 or 101 nodes with uniform spacing. For simplicity, the material constants are $E = 1$, $\rho = 1$. Two Gauss quadrature points are used in each cell. Figure 17 shows the maximal eigenvalues with respect to $D_{\max}$. From the figures we see that the maximum eigenvalues are always bounded by the values given by Equation (137). The ratio of the eigenvalue estimate (137) to the numerical eigenvalue approaches 1.1 as the domain of influence increases.

5.2. Maximum eigenvalue bound of two-dimensional EFG

In a two-dimensional wave problem, the lumped mass matrix at quadrature point Q is

$$\mathbf{M}^{Q}_{\mathrm{lump}} = w_Q J_Q \begin{bmatrix} \phi_1 & & & \\ & \phi_2 & & \\ & & \ddots & \\ & & & \phi_N \end{bmatrix} \tag{139}$$

and the stiffness matrix is

$$\mathbf{K}^{Q} = w_Q J_Q c^2 \begin{bmatrix} \phi_{1,x}\phi_{1,x} + \phi_{1,y}\phi_{1,y} & \cdots & \phi_{1,x}\phi_{N,x} + \phi_{1,y}\phi_{N,y} \\ \phi_{2,x}\phi_{1,x} + \phi_{2,y}\phi_{1,y} & \cdots & \phi_{2,x}\phi_{N,x} + \phi_{2,y}\phi_{N,y} \\ \vdots & & \vdots \\ \phi_{N,x}\phi_{1,x} + \phi_{N,y}\phi_{1,y} & \cdots & \phi_{N,x}\phi_{N,x} + \phi_{N,y}\phi_{N,y} \end{bmatrix} \tag{140}$$

We note that the stiffness matrix $\mathbf{K}^{Q}$ is of rank 2 so there are only two non-zero eigenvalues.

If the nodes are uniformly distributed in both x- and y-direction and the shape functions are symmetric (provided the weight function is symmetric), we have

$$\sum_{I=1}^{N} \phi_{I,x}\phi_{I,y} = 0 \tag{141}$$

The two eigenvalues and corresponding eigenvectors associated with $\mathbf{K}^{Q}$ and $\mathbf{M}^{Q}_{\text{lump}}$ are

$$\lambda_1^{Q} = c^2 \sum_{I=1}^{N} \frac{\phi_{I,x}^2(\mathbf{x}_Q)}{\phi_I(\mathbf{x}_Q)}, \quad \mathbf{v}_1^{Q} = \left[\frac{\phi_{1,x}}{\phi_1} \quad \frac{\phi_{2,x}}{\phi_2} \quad \cdots \quad \frac{\phi_{N,x}}{\phi_N} \right]^{\mathrm{T}}_{\mathbf{x}_Q} \tag{142}$$

$$\lambda_2^{Q} = c^2 \sum_{I=1}^{N} \frac{\phi_{I,y}^2(\mathbf{x}_Q)}{\phi_I(\mathbf{x}_Q)}, \quad \mathbf{v}_2^{Q} = \left[\frac{\phi_{1,y}}{\phi_1} \quad \frac{\phi_{2,y}}{\phi_2} \quad \cdots \quad \frac{\phi_{N,y}}{\phi_N} \right]^{\mathrm{T}}_{\mathbf{x}_Q} \tag{143}$$

Therefore the eigenvalues for the discrete equation are bounded by

$$\lambda^{Q} \leqslant \max(\lambda_1^{Q}, \lambda_2^{Q}) = c^2 \max\left(\sum_{I=1}^{N} \frac{\phi_{I,x}^2}{\phi_I}, \sum_{I=1}^{N} \frac{\phi_{I,y}^2}{\phi_I} \right) \tag{144}$$

If cubic spline function is used as the weight function and the nodal spacings in the x- and y-direction are equal, we have [37]

$$\sum_{I=1}^{N} \frac{\phi_{I,x}^2}{\phi_I} = \sum_{I=1}^{N} \frac{\phi_{I,y}^2}{\phi_I} \approx \frac{\alpha_1}{h^2}, \quad \alpha_1 = 13.30 \tag{145}$$

Then the upper bound for the eigenvalues is

$$\lambda^{Q} \leqslant \alpha_1 \frac{c^2}{h^2} \tag{146}$$

For more general cases where other types of weight functions are used, we numerically obtain an empirical relation for the summation in the upper bound. For example, in this problem we have [37]

$$\sum_{I=1}^{N} \frac{\phi_{I,x}^2}{\phi_I} = \sum_{I=1}^{N} \frac{\phi_{I,y}^2}{\phi_I} \approx \frac{\alpha_2}{h^2}, \quad \alpha_2 = 15.00 \tag{147}$$

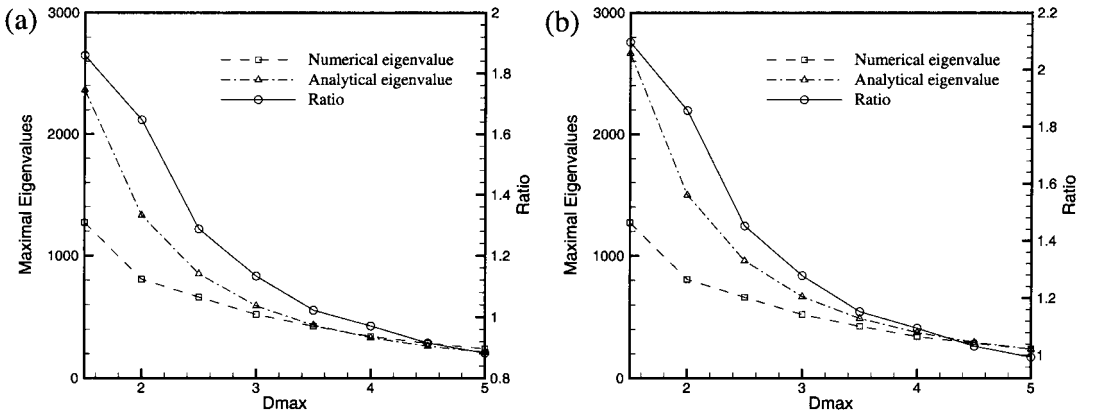

Figure 18. Maximal eigenvalues of two-dimensional wave equation with EFG: (a) upper bound given by Equation (146); and (b) upper bound given by Equation (149).

Then another upper bound for the wave equation is

$$\lambda^Q \leqslant \alpha_2 \frac{c^2}{h^2} \tag{148}$$

To examine this estimate we consider a numerical example on a square with width of 1. A total number of $21 \times 21 = 441$ nodes are uniformly distributed within the square. A cell structure which is coincident with the nodes is used and 2×2 quadrature is used in each cell. Figure 18 shows the maximal eigenvalues for the wave equation. Equation (146) gives better upper bound for small $D_{\max}$ but the analytical eigenvalues are less than the numerical ones for $D_{\max} > 3.5$. The eigenvalues given by Equation (148) are larger than the numerical ones except for $D_{\max} = 5.0$.

6. NUMERICAL EXAMPLES

6.1. Taylor bar impact

The first example is the Taylor bar problem, in which a cylindrical bar impacts a rigid surface, as shown in Figure 19(a). The radius of the cylinder is 3.2 mm and its height is 32.4 mm. The initial velocity of the cylinder is 227 m/s. Von Mises J_2 flow theory with linear isotropic hardening is applied for the computation. The material constants are given as $\rho = 8930$ kg/m^3, $E = 117$ GPa, $v = 0.35$, $E_p = 100$ MPa, $\sigma_Y = 400$ MPa.

Since the problem is axisymmetric, axisymmetry formulation of the governing equations is used and only half of the cylinder is discretized with uniformly distributed particles (see Figure 19(b), where the filled circles indicate boundary nodes). It should be noted that the particles are not placed on the boundary lines.

Two meshless methods, EFG with full cell integration and nodal integration with stress points, are used to solve the problem. The response is computed to 80 μs. In EFG with cell integration, the cell structure is coincident with the nodes and 2×2 quadrature rule is used in each cell. The problem is solved with 20×50 nodes and a time step $\Delta t = 0.005$ μs. So 20×200 particles are used for stress point integration. The stress points can be located either at the centre

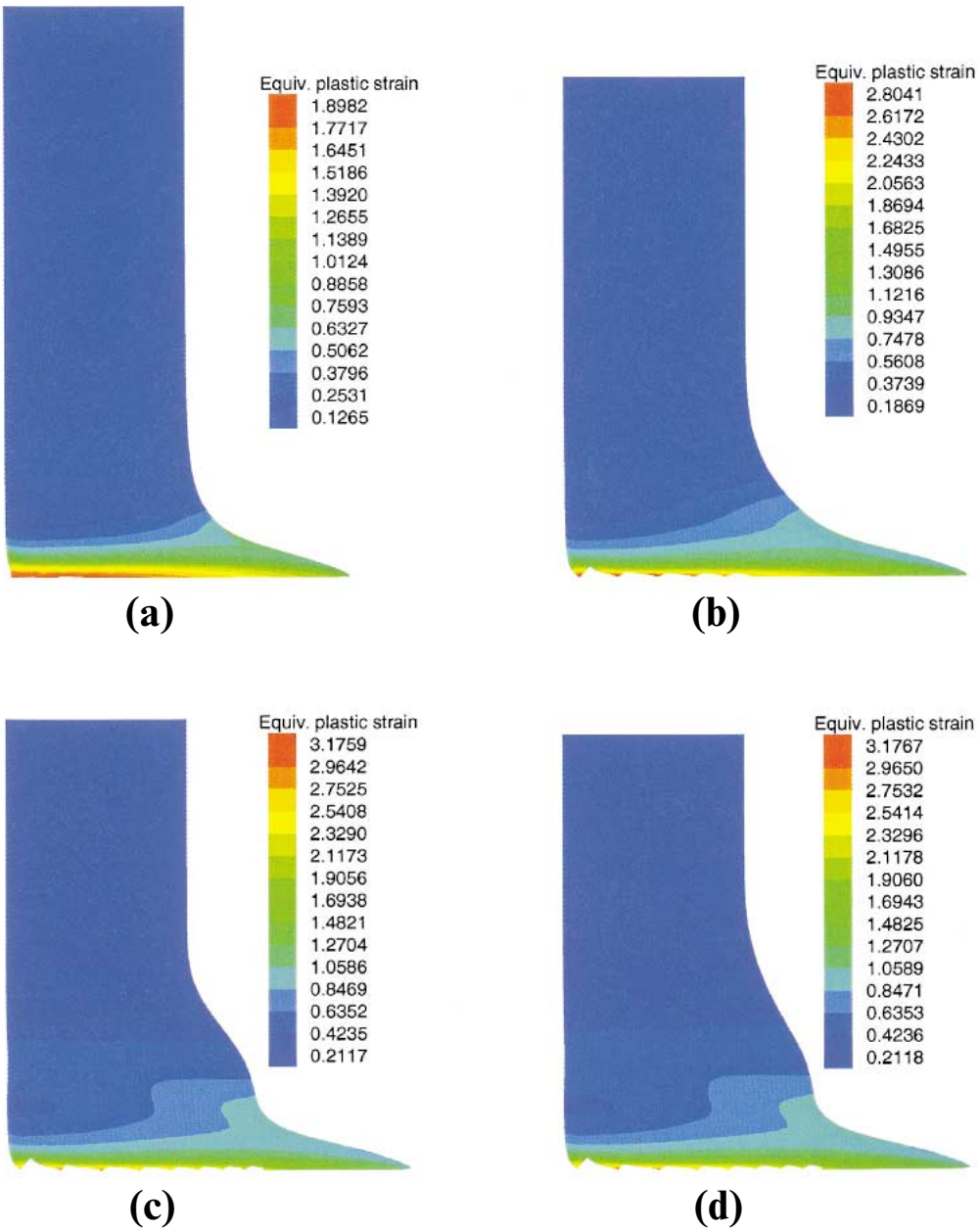

Plate 1. Deformed shape and equivalent plastic strain of a Taylor bar with EFG stress points: (a) 20 μsec; (b) 40 μsec; (c) 60 μsec; and (d) 80 μsec.

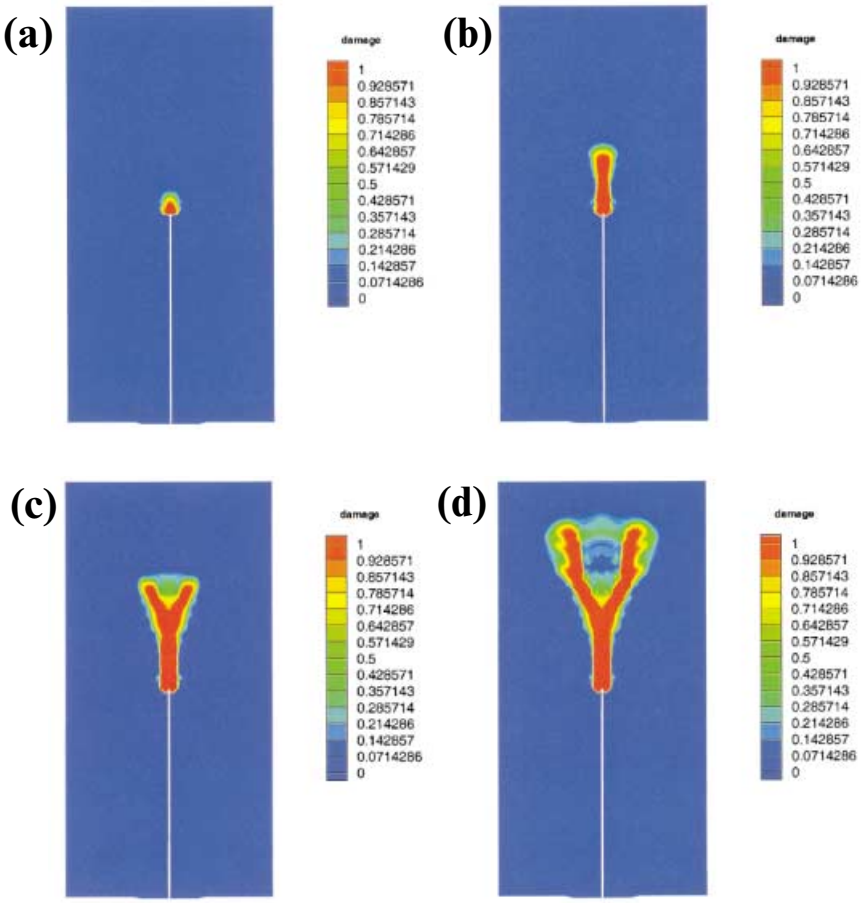

Plate 2. Crack propagation in a finite plate: (a) t = 15 (μsec); (b) t = 30 (μsec); (c) t = 45 (μsec); and (d) t = 60 (μsec).

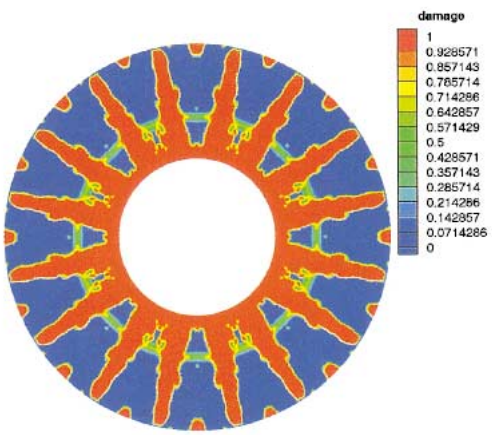

Plate 3. Damage zone in a disk (t = 1.0 msec)

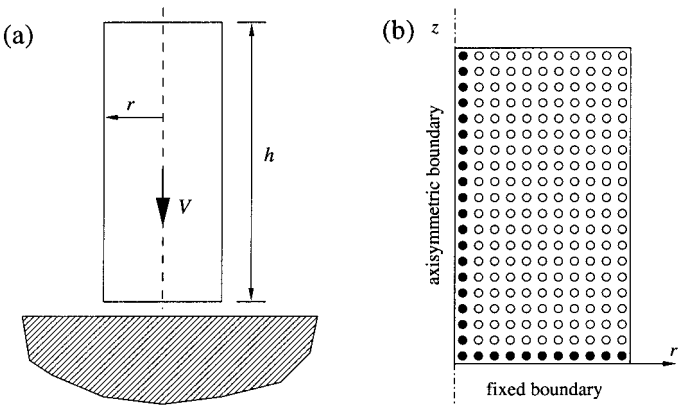

Figure 19. Normal impact of a Taylor bar with particle method: (a) schematic model; and (b) particle discretization.

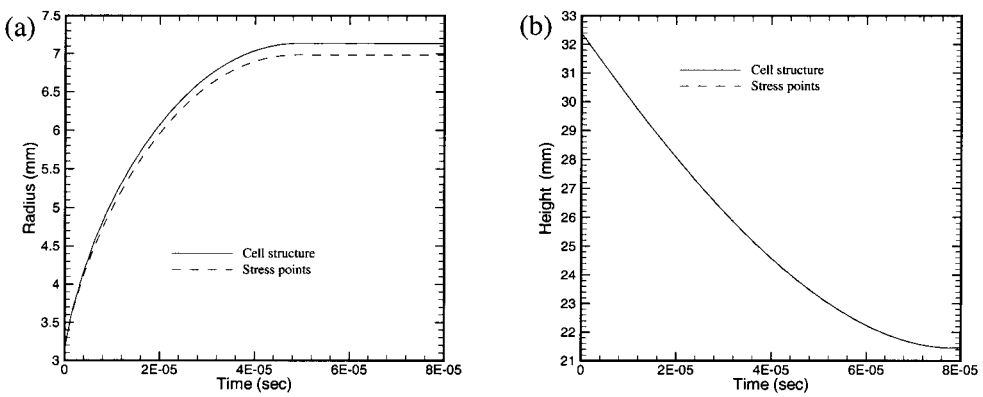

Figure 20. Time history of the radius and height of a Taylor bar: (a) radius at impact surface; and (b) height of the bar.

of quadrilateral or centre of triangle; both implementations yield almost identical results. The results shown here are obtained with the stress points at the centre of quadrilateral. The time step is $\Delta t = 0.005$ μs. The parameter for the domain of influence for these meshless methods is the same, $D_{\mathrm{mx}} = 2.0$.

The time histories of the radius at the contacting surface and the height of the bar are given in Figure 20. The results at $t = 80$ μs are compared with the solution of Hallquist [38] computed by DYNA3D. The radius at the impact plane is 7.13 mm by the full cell integration and 6.98 mm by the stress point integration (DYNA3D: 7.03 mm). The height of the bar is 21.46 mm by both cell integration and stress point integration (DYNA3D: 21.47 mm).

The deformed shape of the bar and the contour plot of the equivalent plastic strain at four different times are shown in Plate 1. The maximum of the equivalent plastic strain is 3.33 by the cell integration and 3.18 by the stress point integration (DYNA3D: 2.96). The meshless

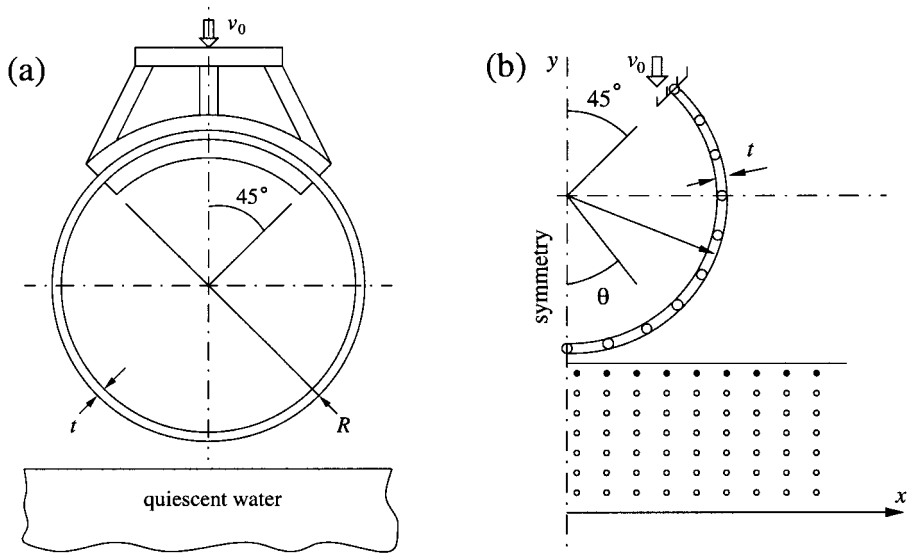

Figure 21. Fluid–structure interaction: (a) schematic model; and (b) computational model.

Table III. Material parameters for structure–fluid interaction.

Structure: steel	Fluid: water, compressible and inviscid
$\rho = 7.8\ \mathrm{g/cm^3}$	
$E = 2.3297 \times 10^{12}\ \mathrm{dyn/cm^2}$	$\rho = 1.0\ \mathrm{g/cm^3}$
$\nu = 0.35$	$B = 2.0 \times 10^{10}\ \mathrm{dyn/cm^2}$
$\sigma_Y = 2.606 \times 10^{9}\ \mathrm{dyn/cm^2}$	$\gamma = 7$
$E_p = 2.144 \times 10^{10}\ \mathrm{dyn/cm^2}$	

methods yield larger maximal equivalent plastic strain than finite elements, but the discrepancy is small.

6.2. *Fluid-structure impact*

The second example is the impact of a circular cylinder into a quiescent pool of water and is designed to simulate the laboratory experiments [39]. The cylindrical shell is supported by clamps over the entire length of the cylinder and is sufficiently long to ensure two-dimensional behaviour. The structure and fluid are shown in Figure 21(a) where $R = 10.48$ cm and $t = 0.08636$ cm.

Due to symmetry only half of the model is simulated. The shell structure is modelled with 25 two-node linear beam elements clamped at the saddle support, as shown in Figure 21(b). The velocity of the structure is prescribed as an initial condition for all nodes and the velocity of the top node is set to the constant driving velocity for the rest of the simulation. The fluid is simulated with 3715 particles and the area of the fluid is 800 cm$\times$ 800 cm. The particles are denser around the impacted area and gradually become coarser. The EFG method with stress point integration

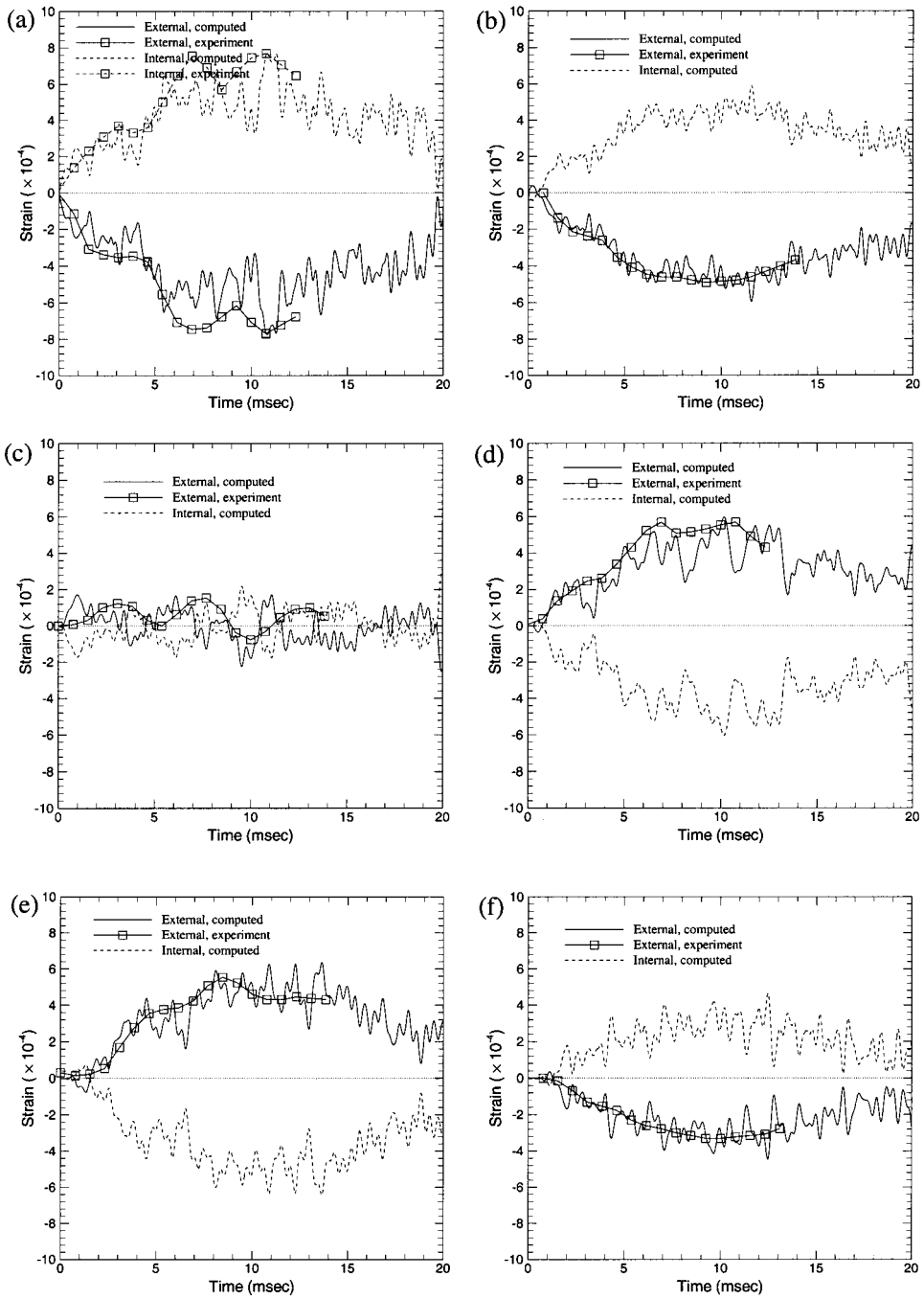

Figure 22. Circumferential strains in shell for 162 cm/s impact: (a) $\theta = 0°$; (b) $\theta = 20°$; (c) $\theta = 40°$; (d) $\theta = 60°$; (e) $\theta = 90°$; and (f) $\theta = 120°$.

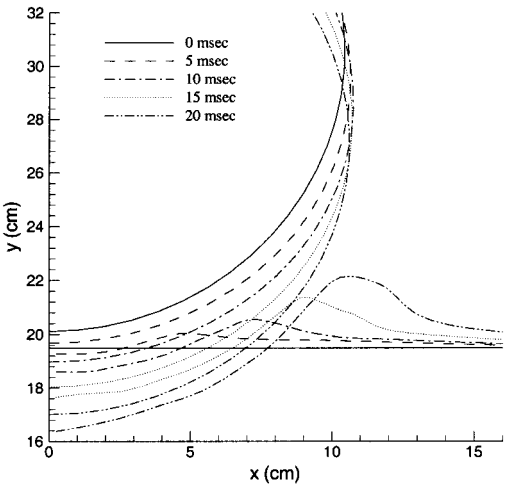

Figure 23. Shape of shell and free surface of fluid for 162 cm/s impact.

is used with the dilation parameter $D_{\mathrm{mx}} = 2.0$ and the stress points located at the center of each triangle (see Figure 12(b)). The total Lagrangian formulation is used.

The material of the shell structure is steel which is simplified to linear isotropic hardening elastoplastic material. The water is modelled as inviscid compressible fluid and the equation of state is [40]

$$p = \frac{B}{\gamma}\left[\left(\frac{\rho}{\rho_0}\right)^{\gamma} - 1\right] \tag{149}$$

The material parameters are given in Table III.

The interaction between the shell structure and the fluid is handled by the pinball contact algorithm [41, 42]. In the fluid, the top layer of particles are selected as pinballs (filled circles in Figure 21(b)). For the structure, each beam element is transformed into a pinball which is always located at the centre of the beam.

The problem is solved with the driving velocity v_0 prescribed as 162 and 369 cm/s. In the former case the shell structure will stay elastic while in the latter case the structure will undergo plastic deformation. The time step is fixed; it is 0.1 μs for low driving speed and 0.05 μs for high impact speed. The computed circumferential strains at several locations in the shell are compared with the experiment given in Reference [39].

Figure 22 shows the computed strains for the 162 cm/s impact, from which we see that these results agree adequately well with the experimental data. At $\theta = 0, 20$ and 120°, the external surface of the shell is in compression and the internal surface is in tension while at locations $\theta = 60$ and 90°, the external surface is in tension. The interesting place is at $\theta = 40°$ where the circumferential strains on external and internal surfaces change signs with the increase of time. The largest discrepance occurs at $\theta = 40°$, where the computed external and internal strains alternate between compression and tension and the maximum strains occur much earlier than in the experiment. The strains at locations other than $\theta = 40°$ become smaller with the time approaching 20 ms, indicating the shell starts to bounce back.

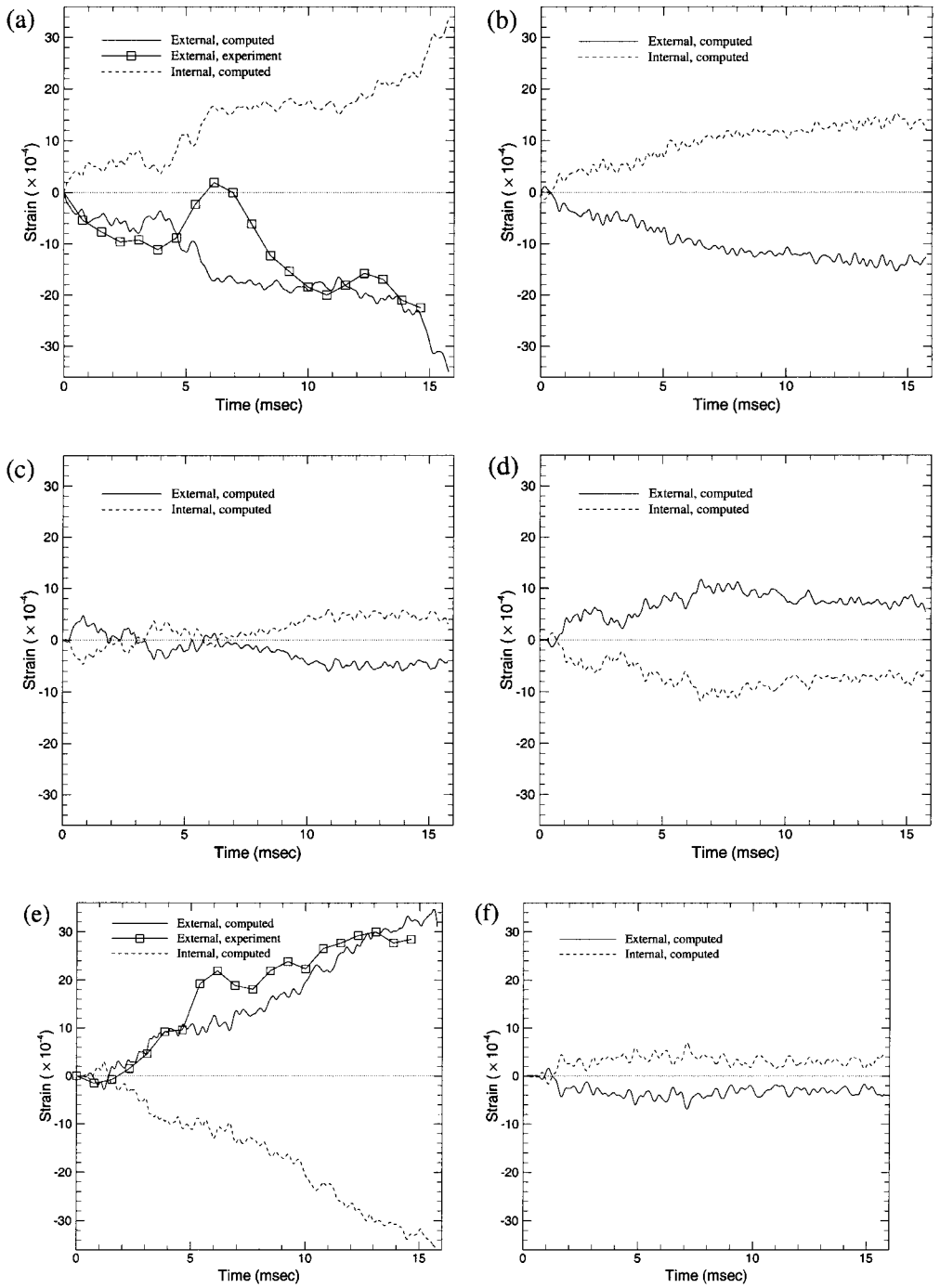

Figure 24. Circumferential strains in shell for 369 cm/s impact: (a) $\theta = 0°$; (b) $\theta = 20°$; (c) $\theta = 40°$; (d) $\theta = 60°$; (e) $\theta = 90°$; and (f) $\theta = 120°$.

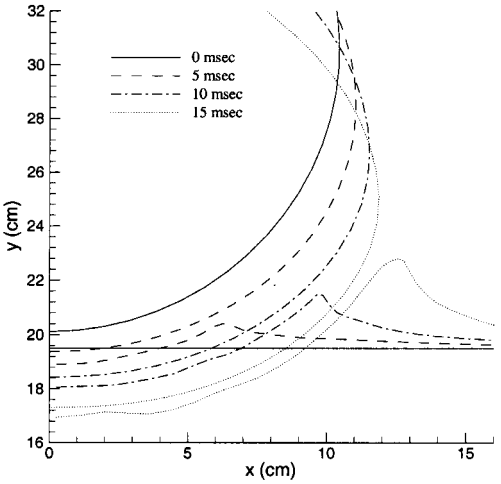

Figure 25. Shape of shell and free surface of fluid for 369 cm/s impact.

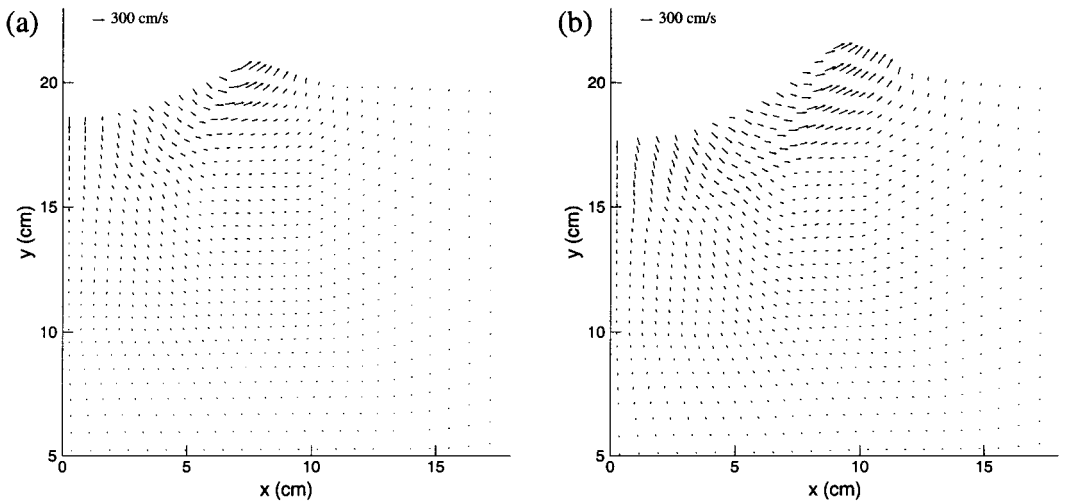

Figure 26. Velocity of fluid particles for 162 cm/s impact: (a) $t = 10$ ms; and (b) $t = 15$ ms.

Figure 23 shows the deformed shape of structure and free surface of fluid at various times. Since these lines are drawn from the positions of the particles or nodes, they do not contact directly with each other. The displacement at the bottom point of the shell in the last two time intervals are larger than the first two, signalling the bouncing back of the shell. This is consistent with the strain profiles.

The computed strains for the 369 cm/s impact are shown in Figure 24. Since the experimental records are available only for $\theta = 0$ and 90°, the comparison between the experiment and computation is given for these locations. For this higher impact velocity, the agreement is not as good as

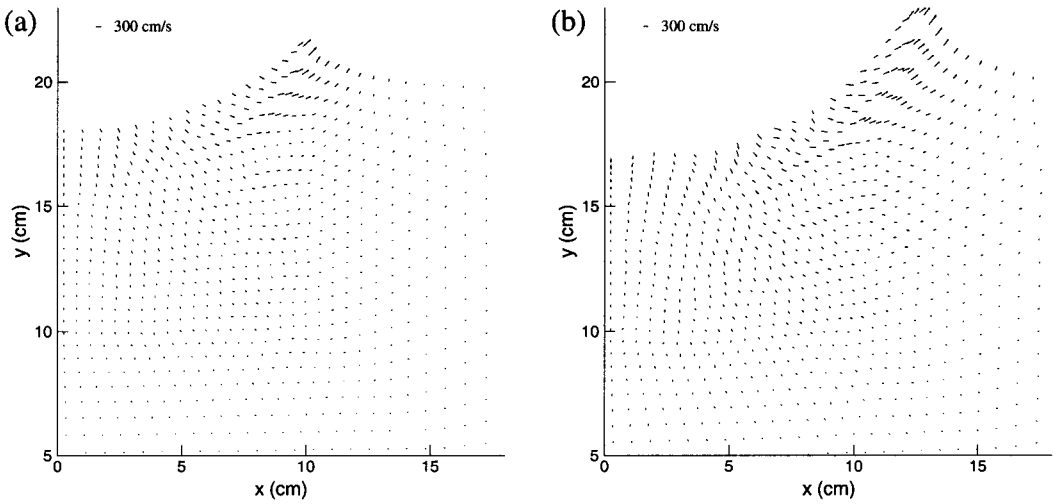

Figure 27. Velocity of fluid particles for 369 cm/s impact: (a) $t = 10$ ms; (b) $t = 15$ ms.

for the lower velocity, and in fact the pronounced drop in strain at about 6 ms at $\theta = 0°$ (Figure 24(a)) is not accurately captured by the computation though there is a drop in computed strains at 4 ms. It can be seen that the strains at locations $\theta = 0$ and 90° change to plastic.

The profiles of the shell and the free surfaces of the fluid are shown in Figure 25 where we can see significant deformation of the shell structure. The velocities of the fluid particles are shown in Figures 26 and 27.

6.3. Damage model

We will use a damage model introduced by Kachanov [43] and developed by Lemaitre [44] for an isotropic linear elastic virgin material to calculate the damage zone propagation in both the plate with a crack and the disk.

The behaviour for a given state of damage is described by

$$\sigma_{ij} = (1 - D)C_{ijkl}\varepsilon_{kl} \tag{150}$$

where D is damage variable which is scalar and its value is in the domain $[0, 1]$. The damage evolution law used as

$$D(\tilde{\varepsilon}) = 1 - \frac{\varepsilon_{D_0}(1 - A_t)}{\tilde{\varepsilon}} - \frac{A_t}{\exp[B_t(\tilde{\varepsilon} - \varepsilon_{D_0})]} \tag{151}$$

where ε_{D_0} is the initial damage threshold strain, and A_t, B_t are characteristic parameters of the material. $\tilde{\varepsilon}$ is the non-local value of the equivalent strain which is defined as

$$\tilde{\varepsilon} = \sqrt{\sum_i \langle \varepsilon_i \rangle_+^2} \tag{152}$$

$\langle \varepsilon_i \rangle_+$ is positive part of the principal strain ε_i.

The first case is a finite plate containing a horizontal crack emanating from the edge with the crack tip centred in the plate. The length and width of the plate are 0.1 and 0.04 m. There are tensile tractions ($\sigma = 1.0$ Mpa) on the two sides of the plate. The material constants are given as $\rho = 2450$ kg/m^3, $E = 32$ GPa, $v = 0.2$, $\varepsilon_{D_0} = 8.5 \times 10^{-5}$, $A_t = 1.0$ and $B_t = 7300$. To solve this problem, we use EFG Lagrangian kernel.

We define the crack as where the damage variable is equal to 1. So, the damage zone evolution, which is shown in Plate 2, is the crack propagation. In Plate 2(c) and (d), there is a branching for the crack propagation. We think it is because the stress waves are reflected by the boundary and they interact with each other.

The second case is a disk whose radius is 0.2 m and there is a hole whose radius is 0.08 m. An initial radial velocity is prescribed along the hole. The material constants are given as $\rho = 5000$ kg/m^3, $E = 1.0$ GPa, $v = 0.2$, $\varepsilon_{D_0} = 1.7 \times 10^{-3}$, $A_t = 1.0$ and $B_t = 2600$.

Plate 3 is the damage zone of the disk at time $t = 1.0$ ms. At the beginning, there is a compressive wave which propagates radially outward. The compressive wave is reflected by the boundary as a tensile wave. The interaction of the tensile and compressive waves results in a damage zone which travels radially outward.

7. CONCLUSIONS

A stability analysis of meshless particle methods was performed. The stability properties of EFG and SPH with Eulerian and Lagrangian kernels under different quadrature schemes were investigated using Fourier analysis. The stability of the least-squares stabilization proposed by Beissel and Belystchko [25] was also studied.

We have shown that in a plane-wave one-dimensional analysis, three types of instability occur in the particle methods:

(i) An instability which occurs due to rank deficiency of the discretization of the divergence and makes the equilibrium equations singular; this occurs regardless of the value of the stress.
(ii) A tensile instability which occurs when the stress is tensile and the second derivative of the kernel large enough.
(iii) An instability under compressive stress; this instability also occurs in the continuum equations so the discretization's capability to mimic this instability is desirable.

Several findings are note worthy:

(i) The tensile instability can be eliminated by using a Lagrangian kernel, i.e. by letting the kernel be a function of the material (Lagrangian) co-ordinates.
(ii) Even in one dimension, stress points do not eliminate the tensile instability for Eulerian kernels, and they fail to eliminate the instability due to rank deficiency for large dilations.
(iii) The least-squares stabilization by Beissel and Belystchko [25] suppresses the aliasing instabilities for small to moderate dilations but fails for large dilations.

In two dimensions, our studies were limited to anti-plane motion. The studies indicate that stress point stabilization is quite delicate in two-dimensional discretizations. For the straightforward scheme where stress points are placed at the centre of virtual quadrilateral generated by the initial positions of the particles, the rank deficiency instability persists. For adequate stabilization of this

spurious mode, stress points must be placed in virtual triangles generated by particle positions, i.e. the density of the stress points must be greater than that resulting from virtual quadrilaterals. The implications of this finding to three-dimensional stress point stabilization require further study.

From the above conclusions, it appears that the best approach to stable particle discretizations of solids and fluids is to use Lagrangian kernels with stress points. Even in the absence of stress points, Lagrangian kernels eliminate the tensile instability. With careful placement of stress points, instabilities can be avoided in multi-dimensional problems.

Eulerian kernels with stress points can also be used, but judiciously. The stress required for the onset of tensile instability is increased by stress points, and in most solids this level of tensile stress is sufficient for fracture. Thus, if a reasonable constitutive equation is used, the tensile instability can be avoided. However, care must be taken in fluids, for as shown in this paper, even with stress point stabilization, the aliasing mode can occur in Eulerian kernels if the dilation becomes large.

Estimates for the stable time step for central difference time integration were also presented. For uniformly spaced particles the maximum frequency obtained from the Fourier analysis can be used to evaluate the critical time step. For arbitrary spacing, the eigenvalue inequalities yield a conservative estimate on the upper bound of the maximal eigenvalue. Closed-form expressions of the upper bounds for one- and two-dimensional EFG were obtained.

ACKNOWLEDGEMENTS

The support of Army Research Office and Office of Naval Research, the Army High Performance Computing Research Center under the Auspices of the Department of the Army, Research Laboratory Cooperative Agreement DAAH04-95-2-003/Contract DAAH04-95-C-0008, is gratefully acknowledged.

REFERENCES

1. Lucy LB. A numerical approach to the testing of the fission hypothesis. *Journal of Astronomy* 1977; **82**:1013–1024.
2. Gingold RA, Monaghan JJ. Smoothed particle hydrodynamics: theory and application to non-spherical stars. *Monthly Notice of the Royal Astronomical Society* 1977; **181**:375–389.
3. Mas-Gallic S, Raviart P. A particle method for first-order symmetric systems. *Numerische Mathematik* 1987; **51**: 323–352.
4. Belytschko T, Krongauz K, Dolbow J, Gerlach C. On the completeness of meshfree particle methods. *International Journal for Numerical Methods in Engineering* 1998; **43**:785–819.
5. Liu WK, Jun S, Zhang Y-F. Reproducing kernel particle methods. *International Journal for Numerical Methods in Fluids*, 1995; **21**:901–931.
6. Krongauz K, Belytschko T. Consistent pseudo-derivatives in meshless methods. *Computer Methods in Applied Mechanics and Engineering* 1997; **146**:371–386.
7. Randles P, Libersky L. Smoothed particle hydrodynamics: some recent improvements and applications. *Computer Methods in Applied Mechanics and Engineering* 1996: **139**:375–408.
8. Belytschko T, Lu Y-Y, Gu L. Element-free Galerkin methods. *International Journal for Numerical Methods in Engineering* 1994; **37**:229–256.
9. Belytschko T, Krongauz K, Organ D, Fleming M, Krysl P. Meshless methods: an overview and recent developments. *Computer Methods in Applied Mechanics and Engineering* 1996; **139**:3–47.
10. Liu WK, Chen Y, Chang C-T, Belytschko T. Advances in multiple scale kernel particle methods. *Computational Mechanics* 1996; **18**(2):31–111.
11. Hockney R, Eastwood J. *Computer Simulation Using Particles*. McGraw-Hill: New York, 1981.
12. Harlow FH. PIC and its progeny. *Computer Physics Communications* 1988; **48**:1.
13. Duarte CA, Oden JT. Hp clouds—a meshless method to solve boundary-value problems. *Technical Report 95-05*, University of Texas at Austin, 1995.
14. Duarte CA, Oden JT. An H-P adaptive method using clouds. *Computer Methods in Applied Mechanics and Engineering* 1996; **139**:237–262.

15. Melenk JM, Babuška I. The partition of unity finite element method: basic theory and applications. *Computer Methods in Applied Mechanics and Engineering* 1996; **139**:289–314.
16. Babuška I, Melenk JM. The partition of unity finite element method. *International Journal for Numerical Methods in Engineering* 1997; **40**:727–758.
17. Swegle JW, Hicks DL, Attaway SW. Smoothed particle hydrodynamics stability analysis. *Journal of Computational Physics* 1995; **116**:123–134.
18. Dyka CT, Ingel RP. An approach for tension instability in smoothed particle hydrodynamics (SPH). *Computers and Structures*, 1995, **57**:573–580.
19. Dyka CT, Randles PW, Ingel RP. Stress points for tension instability in SPH. *International Journal for Numerical Methods in Engineering* 1997; **40**:2325–2341.
20. Dilts GA. Moving-least-squares-particle hydrodynamics: I. Consistency and stability. *International Journal for Numerical Methods in Engineering* 1999; **44**:1115–1155.
21. Swegle JW, Attaway SW, Heinsein MW, Mello FJ, Hicks DL. An analysis of smoothed particle hydrodynamics. *Report No. SAND93-2513-UC-705*, Sandia National Laboratories, Albuquerque, NM, 1994.
22. Wen Y, Hicks DL, Swegle JW. Stabilizing SPH with conservative smoothing. *Report No. SAND94-1932-UC-705*, Sandia National Laboratories, Albuquerque, NM, 1994.
23. Morris JP. A study of the stability properties of SPH, *Applied Mathematics Reports and Preprints*, Monash University, 1994.
24. Morris JP. A study of the stability properties of smoothed particle hydrodynamics. *Publications of the Astronomical Society of Australia* 1996; **13**.
25. Beissel S, Belytschko T. Nodal integration of the element-free Galerkin method. *Computer Methods in Applied Mechanics and Engineering* 1996; **139**:49–74.
26. Hill R. *Journal of the Mechanics and Physics of Solids* 1962; **10**:1.
27. Rice JR. In *Theoretical and Applied Mechanics*, Koher WT (ed.). North-Holland: Amsterdam, 1977; **207**.
28. Rudnicki JW, Rice JR. *Journal of the Mechanics and Physics of Solids*, 1975; **23**:371.
29. Belytschko T, Liu WK, Moran B. *Finite Element Methods for Nonlinear Continua and Structures*. Wiley: New York, 2000, to be published.
30. Krongauz K, Belytschko T. Enforcement of essential boundary conditions in meshless approximations using finite elements, *Computer Methods in Applied Mechanics and Engineering* 1996; **131**:133–145.
31. Belytschko T, Krongauz K, Fleming M, Organ D, Liu WK. Smoothing and accelerated computations in the element-free Galerkin method. *Journal of Computational and Applied Mathematics* 1996; **74**:111–126.
32. Monaghan JJ. An introduction to SPH. *Computer Physics Communications* 1988; **48**:89–96.
33. Bonet J, Lok T-SL. Variational and momentum preserving aspects of smoothed particle hydrodynamics (SPH) formulations. *Computer Methods in Applied Mechanics and Engineering* 1999; **180**(1-2):97–116.
34. Seydel R. *From Equilibrium to Chaos*, *Practical Bifurcation and Stability Analysis*. Elsevier: New York, 1988.
35. Thompson JMT, Hunt GW. *Elastic Instability Phenomena*. Wiley: New York, 1984.
36. Belytschko T, Ong J-S, Liu WK, Kennedy JM. Hourglass control in linear and nonlinear problems. *Computer Methods in Applied Mechanics and Engineering* 1984; **43**:251–276.
37. Guo Y. Composite finite elements and stabilization of meshfree methods. *Ph.D. Dissertation*, Northwestern University, Evanston, IL, 1999.
38. Hallquist JO. DYNA2D and DYNA3D user's manuals. *Technical Report*, Lawrence Livermore National Laboratories, Livermore, CA, 1980.
39. Souter K, Krachman H. Two-dimensional water-impact tests of flexible cylinders. *EPRI Report NP*-1612, November, 1980.
40. Monaghan JJ. Simulating free surface flows with SPH. *Journal of Computational Physics* 1994; **110**:399.
41. Belytschko T, Neal MO. The vectorized pinball contact-impact routine. In *Transactions of the 10th International Conference on Structural Mechanics in Reactor Technology*, Los Angeles, CA, Hadjian AH (ed.), Vol. B. AASMiRT: Anaheim, CA, 1989; 161–166.
42. Belytschko T, Neal MO. Contact-impact by the pinball algorithm with penalty and Lagrangian methods. *International Journal for Numerical Methods in Engineering* 1991; **31**:547–572.
43. Kachanov LM. Time of the rupture process under creep conditions. *Izvestiya Akademii Nauk SSR Otdelenie Technicheskikh Nauk* 1958; **8**:26–31.
44. Lemaitre J. Evaluation of dissipation and damage in metal submitted to dynamic loading. *Proceedings ICM* 1, Kyoto, Japan, 1971.

